JGR Solid Earth

RESEARCH ARTICLE
10.1029/2024JB028710

Fault (Re)Activation and Fluid-Induced Seismicity: An Example From the Val d'Agri Intermontane Basin (Southern Italy)

Alessio Lavecchia[1], Vincenzo Serlenga[2], Marilena Filippucci[1,3], Tony Alfredo Stabile[2], Giacomo Prosser[4], and Andrea Tallarico[1,3]

[1]University of Bari, Bari, Italy, [2]National Research Council of Italy, Institute of Methodologies for Environmental Analysis, Tito Scalo, Italy, [3]National Institute of Geophysics and Volcanology, Rome, Italy, [4]University of Basilicata, Potenza, Italy

Key Points:

- We propose a numerical thermo-mechanical model to identify the mechanisms that promoted the present-day Val d'Agri tectonic setting
- The presence of a décollement layer and reactivation of preexisting faults are key factors for generating seismically active structures
- The Val d'Agri crust stress state indicates the presence of critically stressed faults where fluid pressure increase may trigger seismicity

Supporting Information:

Supporting Information may be found in the online version of this article.

Correspondence to:

A. Lavecchia,
alessio.lavecchia@uniba.it

Citation:

Lavecchia, A., Serlenga, V., Filippucci, M., Stabile, T. A., Prosser, G., & Tallarico, A. (2024). Fault (re)activation and fluid-induced seismicity: An example from the Val d'Agri intermontane basin (southern Italy). *Journal of Geophysical Research: Solid Earth*, *129*, e2024JB028710. https://doi.org/10.1029/2024JB028710

Received 10 JAN 2024
Accepted 15 JUL 2024

Author Contributions:

Conceptualization: Alessio Lavecchia
Data curation: Alessio Lavecchia, Vincenzo Serlenga, Tony Alfredo Stabile, Andrea Tallarico
Formal analysis: Alessio Lavecchia, Marilena Filippucci, Andrea Tallarico
Funding acquisition: Andrea Tallarico
Investigation: Alessio Lavecchia
Methodology: Alessio Lavecchia, Marilena Filippucci, Giacomo Prosser, Andrea Tallarico
Project administration: Andrea Tallarico
Resources: Alessio Lavecchia
Software: Alessio Lavecchia, Andrea Tallarico

Abstract Fluid-induced seismicity has been a particularly emphasized mechanism over the last few years, especially after fluid-related, moderate-to-large earthquakes have been observed in several locations around the globe. Several studies suggest that the relationships between seismicity and fluid presence are related to variations in the stress state of rocks, due to the increase or drop of the pore fluid pressure. In this scenario, the Val d'Agri represents a precious case study where fluid-induced seismicity is observed. In this area, two seismic clusters are observed in the Apulian Carbonate Platform, caused by (a) wastewater reinjection that reactivated the Costa Molina Fault blind thrust, and (b) seasonal water loading from the Pertusillo reservoir. The mechanisms behind these reactivated faults' evolution are still uncertain, especially in the compressive/extensional tectonic setting characterizing the area's evolution. Consequently, the distribution of the seismic potential in the region is largely unconstrained. We constructed a numerical thermo-mechanical model to identify the main mechanisms that promoted the Val d'Agri present-day tectonic setting and to assess the seismic hazard characterizing this region. We show that deformation within the Sedimentary Cover and the Crystalline Basement decoupled along a major décollement layer, represented by the Triassic Burano Formation. We also estimate the Coulomb stress (σ_C) in the region, assessing the crust's potential to generate earthquakes. Our results suggest that $\sigma_C > 0$ in a large part of the crust, and therefore that fluid injection may be particularly effective for the reactivation of buried structures, especially at a depth between ≃2 and ≃6 km.

Plain Language Summary Fluids are one of the elements that can generate seismicity. The Val d'Agri is one of the regions where the injection of wastewater at depth in the subsurface caused the generation of low-magnitude earthquakes in the proximity of the Costa Molina well, while the presence of the Pertusillo Lake led to further seismic activity in the SW area of the valley. This seismicity is generated along faults whose geometry and evolution are still a matter of debate. One of the consequences of this uncertainty is that the seismic hazard that characterizes the Val d'Agri and surrounding regions is not very well constrained. Therefore, we built up a numerical model that identifies the factors leading to the present-day fault configuration and activity in the area. In addition, we provide an estimation for the potential seismic hazard that characterizes the Val d'Agri. We show that the Val d'Agri configuration is largely due to a decoupled deformation of the sedimentary cover with respect to the crystalline basement. In addition, stress field estimations in the region suggest that the Val d'Agri is a high seismic hazard area, where fluid-related human activities in the subsurface should be carried out with caution.

1. Introduction

The continental crust's mechanical behavior has a major impact on the tectonic evolution of the lithosphere (e.g., Gogus & Ueda, 2018; Huismans & Beaumont, 2011; Lavecchia, Beekman, et al., 2016; Lavecchia, Clark, et al., 2016). While the continental crust is subjected to stress stemming from both deep and surface processes, its complex response is due to its space and time variations in the lithological, structural, and physical properties. Consequently, its deformation history is often complex and difficult to predict and therefore many regions around the globe are characterized by complex deformation patterns, whose evolution is still not fully understood (e.g., Corti et al., 2010; Ebinger, 2005; Pedersen et al., 2009; Ranalli, 2000). In such a scenario, numerical models constituted an invaluable investigation tool highlighting how regional tectonics can be the result of several mechanisms acting simultaneously, often at different times and intensities (Ballato et al., 2019; Brune et al., 2017; Burov & Poliakov, 2001; Gerya et al., 2000; Huismans & Beaumont, 2011; Vogt et al., 2013; Waltham, 1992).

Supervision: Andrea Tallarico
Validation: Alessio Lavecchia, Vincenzo Serlenga, Marilena Filippucci, Tony Alfredo Stabile, Giacomo Prosser, Andrea Tallarico
Visualization: Alessio Lavecchia, Vincenzo Serlenga, Tony Alfredo Stabile, Giacomo Prosser
Writing – original draft: Alessio Lavecchia, Andrea Tallarico
Writing – review & editing: Alessio Lavecchia, Vincenzo Serlenga, Tony Alfredo Stabile, Giacomo Prosser, Andrea Tallarico

The presence of fluid phases, either generated by phase changes or coming from an external source, is undoubtedly one of the most prominent elements that can have an impact on the crust's mechanical strength and behavior. As an example, although several aspects of rock-fluid interaction mechanisms still constitute a debated field of research, several previous studies already highlighted the strong weakening effect of fluid phases on rock strength (e.g., Sibson, 2000).

Among the consequences of fluid presence at various depths in the crust, enhanced seismicity is one of the most remarkable (e.g., Audin et al., 2002; Benson et al., 2020; Gardonio et al., 2018). The effect of fluids on seismic activity has been initially related to an increase in pore fluid pressure, that causes a decrease in effective normal stresses and allows fault slip at near-ambient values of shear stress (e.g., Healy et al., 1968; Raleigh et al., 1972, 1976). However, it was also observed in several cases that fluid extraction, and therefore a drop of pore fluid pressure, was accompanied by faulting and seismicity (Yerkes & Castle, 1976), due to the perturbation of the rocks' local state of stress (Segall, 1989). This effect may occur especially on a short time scale, when the presence of interconnected fluid phases decreases the shear stress needed to produce rock failure and favors the likelihood of faulting and sliding (e.g., El Hariri et al., 2010; Ranalli, 1995; Van Dinther et al., 2013). The effect of fluids on rock strength is related to the effect of pore fluid pressure on fault strength, which is quantified by the Coulomb failure stress change law (e.g., Kilb et al., 2002; King et al., 1994; Reasenberg & Simpson, 1992; Toda et al., 2011) and determines a decrease in fault strength when the pore fluid pressure increases (e.g., Nakagomi et al., 2021; Stabile et al., 2021). This effect is further enhanced when fault stress is near failure conditions, and consequently, a small stress increase is enough to cause new ruptures (e.g., Alt et al., 2016). It has been suggested (Harris, 1998; King et al., 1994, and references therein) that changes in pore fluid pressures as low as 0.01 MPa can be locally sufficient to trigger earthquakes.

Previous works have already shown a correlation between fluids and an increase in the seismic hazard in the Apennines region (Talone et al., 2023). In this scenario, the Val d'Agri (VA) (Figure 1) represents a perfect example of how crustal structure and seismic behavior can result from several factors interacting with one another. The VA is delimited by two main systems of high-angle normal faults, namely the Eastern Agri Fault System to the northeast (Cello et al., 2003) and the Mts. Maddalena Fault System to the southwest (Maschio et al., 2005). Extensional tectonics in the uppermost crustal levels is located above km-scale anticlines at a depth between 2 and 6 km (Nicolai & Gambini, 2007). The region is characterized by extensional rates of 2–5 mm/yr (e.g., D'Agostino et al., 2008) and low to average heat flow values (e.g., Megna et al., 2014, and references therein). Several medium to high magnitude earthquakes have occurred in the VA in historical times, that is, the 1857 Mw7 Basilicata earthquake (Boschi et al., 2000), suggesting a high seismogenic potential of the region. In addition, the VA is characterized by important oil reservoirs, that make it the largest productive oil field in Western Europe (Holton, 1999). Several studies highlight the occurrence of artificially induced seismicity, both during and after operations of fluid injections (Albaric et al., 2014; Evans et al., 2005; Hsieh & Bredehoeft, 1981; Stanchits et al., 2011). Similarly, in the VA the relationships between oil exploitation activity and seismicity have been well established in several previous studies and can be both related to oil extraction with progressive depletion of the reservoir (Hager et al., 2021) and disposal of wastewater through pumping at the Costa Molina 2 (CM2) injection well (Buttinelli et al., 2016; Improta et al., 2017; Stabile, Giocoli, Perrone, et al., 2014; Stabile et al., 2021), where fluids are injected back into the same hydrocarbon reservoir in a compartment hydraulically connected to the production area (Stabile & Telesca, 2023). Other mechanisms generating seismicity in the VA are those related to seasonal loading produced by the Pertusillo Lake (PL) artificial reservoir, characterized by seasonal annual fluctuations of around 10–15 m and extreme recorded values of 50 m (Stabile, Giocoli, Lapenna, et al., 2014). The observed seismicity is actually due to mechanisms of pore fluid pressure diffusion (e.g., Stabile, Giocoli, Lapenna, et al., 2014; Stabile et al., 2015; Telesca et al., 2015) as well as to the combined hydraulic and mechanical effects of the loading changes due to the seasonal variations of water level of the lake (e.g., Rinaldi et al., 2020).

According to several geological and geophysical studies (e.g., Butler et al., 2005; Improta & Corciulo, 2006; Mazzoli et al., 2001; Mazzotti et al., 2000; Menardi Noguera & Rea, 2000; Patacca & Scandone, 2001; Scrocca et al., 2003, 2005; Speranza & Chiappini, 2002; Steckler et al., 2008), the mechanisms that generated the current tectonic setting and the related stress field in the VA area are mainly connected to the expansion of the Tyrrhenian back-arc extension in the Southern Apennines region. However, the presence of active faults, their location and their possibility to generate earthquakes are still a matter of debate, especially in the presence of a fluid circulation system (Improta et al., 2014; Maschio et al., 2005). For this purpose, we constructed a 2D thermo-mechanical

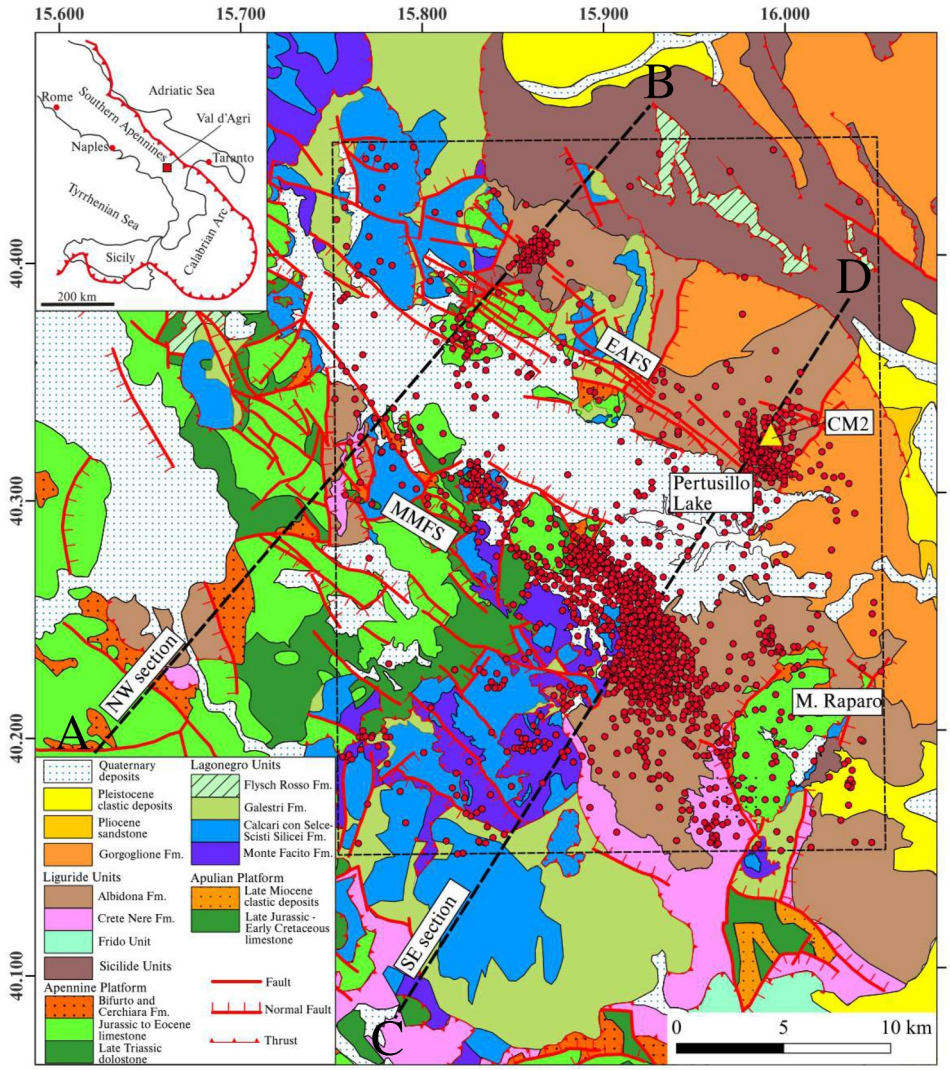

Figure 1. Schematic geological map of the VA. Data are taken from Bonardi et al. (1988), Carbone et al. (1991), Maschio et al. (2005), and Palladino et al. (2023). The red lines define the main fault systems observed in the region (EAFS: Eastern Agri Fault System; MMFS: Mts. Maddalena Fault System). The black dotted box encloses the region where seismicity has been used for the model validation. The red dots represent the position of the earthquake epicenters recorded in the study area. The black dashed lines have a length of 40 km, corresponding to the region of the model going from $x = 40$ km to $x = 80$ km in Figure 2, and indicate the profiles simulated in case B (segment A-B) and C (segment C-D).

model taking into account the effect that temperature, lithology, kinematic variations and fluids can exert on rock strength and deformation. The need for a careful evaluation of the hazard connected to fluid-induced seismicity has already been highlighted in previous numerical models in several regions around the globe (e.g., Baisch et al., 2010; Deng et al., 2021; Hearn et al., 2018; Maurer et al., 2020; Yoon et al., 2017). In addition, the study by Hager et al. (2021) addressed the issue of the presence and level of activity of faults within the VA region by coupled flow, geomechanical and earthquake models. This study, however, relies upon the mapping and interpretation of faults either recognized by the authors or shown in previous studies, with in situ stress conditions derived from borehole breakouts and induced fractures. Consequently, the possibility of unknown faults and uncertainty of fault geometry in the subsoil are factors to be taken into account. On the other hand, our study reproduces the evolution of the valley's structural setting, therefore providing information on the present-day faults' characteristics. With this model, we aim to better assess the factors leading to the present-day structure of the region and their interactions. In addition, it provides an evaluation of the stress field affecting the VA,

allowing us to reconstruct the relationships between stress, rheology, faults and fluids in the region and to estimate the seismic hazard connected to fluid-related seismicity in the valley and surrounding areas.

2. Geological Setting

The VA is a Quaternary, WNW-ESE elongated intermontane basin. It is located in the axial part of the Southern Apennines thrust and fold belt, which originated from the Miocene to early Pleistocene contractional tectonics, resulting from the collision of the African and Eurasian lithospheric plates (e.g., Aliaj, 2006; Malinverno & Ryan, 1986; Menardi Noguera & Rea, 2000; Patacca et al., 1990; Stein & Sella, 2006). The Southern Apennines evolution is characterized by a polyphase tectonic history, that reflects on the mountain belt's stratigraphic and structural configurations. The formation of the Southern Apennines is predated by an extensional phase (e.g., Mattavelli et al., 1991; Stampfli, 2005; Stampfli et al., 2002, and references therein) that led to the deposition of Paleozoic-Triassic sediments above the Crystalline Basement (CB) (Patacca et al., 2008) and, subsequently, to the deposition of a thick shallow water carbonate platform between late Triassic and late Cretaceous (e.g., Del Ben et al., 2010; Scrocca, 2010, and references therein) and its separation by a deep water basin filled with siliclastic, siliceous and carbonatic sediments that, at the present day, constitute the Lagonegro units (Cello & Mazzoli, 1998).

Since the late Cretaceous, N-S and NE-SW shortening phases, connected to the Eurasia-Africa plate convergence, were responsible for the formation of the Liguride accretionary complex, with the subsequent involvement of the Apennine sector of the carbonate platform and the Lagonegro units in the contractional deformation during the Middle Miocene. These Units overrode the Apulian sector of the carbonate platform starting from the late Miocene (e.g., Butler et al., 2005; Cello & Mazzoli, 1998). Afterward, the Miocene to Quaternary evolution has been characterized by the eastward slab roll-back (Doglioni et al., 1996) that caused extension in the Tyrrhenian basin (Buiter et al., 1998, and references therein) and the eastward migration not only of the thrusts fronts, as testified by the presence of several piggy-back basins developed on top of the allochthonous units, but also of the backarc tectonics, that affected inland mountain basins at the rear of the accretionary wedge (e.g., Doglioni, 1991; Malinverno & Ryan, 1986; Patacca & Scandone, 2001; Patacca et al., 1990).

The VA is bordered by two main fault systems, namely the Eastern Agri Fault System and the Mts. Maddalena Fault System, although the activity of either of the systems is still not well defined (Cello et al., 2003; Maschio et al., 2005). This basin is filled with Quaternary continental deposits overlying a sequence constituted, from the top to the bottom, by (a) a pre-Quaternary substratum consisting of allochthonous units, (b) a $\simeq$7 km thick carbonate formation of the Apulian Carbonate Platform (ACP), (c) Triassic evaporite formation (Burano Formation (BF)), and (d) the crystalline basement (Doglioni et al., 1999; Scrocca et al., 2005; Valoroso et al., 2011, and references therein). The allochthonous units consist of Mesozoic-Paleogene carbonate platform and pelagic basin units (Lagonegro Units), unconformably overlaid by Tertiary siliciclastic sediments (Gorgoglione Flysch and Albidona Formation) (e.g., Buttinelli et al., 2016, and references therein). A layer of primary interest is constituted by a melange zone at the base of the Allochthonous units (AU) several hundred meters thick and mostly made up of mudstone and siltstone (Mazzoli et al., 2001). This layer has been interpreted as a level of décollement between the AU and the ACP. In addition, it acted as a seal for the migration of deep fluids (i.e., oil) toward the surface (Stabile, Giocoli, Perrone, et al., 2014).

After a period of compression, coherently with the shortening experienced by the Southern Apennines, the VA is undergoing extension at a rate of a few mm/yr (Amato & Montone, 1997; D'Agostino et al., 2008) since at least the Middle Pleistocene (Cinque et al., 1993). In this framework, the role of the border faults is still a matter of debate. Field and geophysical surveys (e.g., Benedetti et al., 2002; Cello et al., 2003; Colella et al., 2004) highlight a remarkable role of the Eastern Agri Fault System in driving the basin opening. On the other side, other studies suggest that the most recent basin evolution is controlled by motion along the Mts. Maddalena Fault System, recognizing its seismogenic potential (Maschio et al., 2005; Morandi & Ceragioli, 2002; Zembo, 2010).

3. The Model

3.1. General Aspects

The model aims to identify the main mechanisms that controlled the structural evolution of the VA and caused or promoted the present-day seismic pattern. For this purpose, we reproduced the compressional/extensional history

of the VA and surrounding region during the Quaternary (Figure 2). We have chosen this time period because by the early Pleistocene the Apulian Platform has been tectonically buried by the allochthonous wedge (Ascione et al., 2012), allowing us to approximate the latter as a single layer overlying the carbonates at the onset of the simulation. In addition, 2.6 Myr is a much larger period than the Maxwell relaxation time of the crust (Bailey, 2006; Curbelo et al., 2019). Therefore, with these assumptions, we can consider the crust as a highly viscous fluid.

We carried out simulations using the open-source code ASPECT 2.3.0 (Kronbichler et al., 2012). ASPECT is a code based on the Finite Element Method, designed to solve geodynamic problems by describing the motion of highly viscous materials with complex, nonlinear rheology, driven by gravitational instability. The parameters adopted in the entire model are given in Table 1. The VA crust is modeled as a 2D, stratified rectangular domain Ω with an extension $W_M = 120$ km and an initial thickness $H_M = 20$ km (Figure 2a), roughly corresponding to a SW-NE section cross-cutting the valley and subperpendicular to the Southern Apennines. The chosen extension of the model is much larger than the VA extension, therefore any possible boundary conditions-related numerical artifacts do not affect results in our region of interest. The VA crust is modeled with visco-plastic rheology, it deforms under an applied velocity field at the boundaries (Figure 2b) and is subjected to erosion/sedimentation. The VA region covers a subrectangular domain with dimensions ≃25 km in the NW-SE direction, subparallel to the Southern Apennines ridge, and ≃10 km in the NE-SW direction. The velocity field in the Southern Apennines and the Adria microplate shows variations on a much larger spatial scale than the VA dimensions (e.g., D'Agostino, 2014). Consequently, the choice of a 2D domain is appropriate for the study area. We have chosen the size of the element composing the mesh by conducting sensitivity tests with increasingly smaller elements. More specifically, we have carried out simulations where we gradually increased the number of nodes composing each km of our domain in both the x and z directions, and then we compared the results. Our tests show that, when 7 or more nodes per km are implemented (corresponding to a mesh size of ≃140 m), there are no remarkable variations in the simulations' outcomes (Figure S1 in Supporting Information S1).

The reliability of the model results is reached when simulations with appropriate initial and boundary conditions provide estimates of geological and geophysical observables that are comparable with the available data. We consider vertical surface heat flow, topography, seismicity, strain rate, and structural setting as test observables for the study area. Particularly, we quantify the seismic potential of the faults generated in our simulations, taking into account the effect of fluids on the Coulomb stress σ_C variations for fault activation.

3.2. Model Equations

3.2.1. Momentum Conservation

The motion equation for a continuum medium is given by

$$\nabla \cdot \boldsymbol{\sigma} + \rho \mathbf{g} = \rho \frac{D\mathbf{v}}{Dt} \tag{1}$$

where $\nabla \cdot \boldsymbol{\sigma}$ is the divergence of the stress tensor $\boldsymbol{\sigma}$, ρ is the density, $\mathbf{g}$ is the acceleration of gravity, $\frac{D}{Dt}$ is the total derivative with respect to the time t and $\mathbf{v}(\mathbf{x}, t)$ is the velocity. The two terms on the left-hand side of the equation represent the surface and body forces respectively, whereas the term on the right-hand side is the inertial term.

The Navier-Stokes equation is obtained by substituting $\boldsymbol{\sigma}$ in Equation 1 with the rheological law:

$$\boldsymbol{\sigma} = -p\mathbf{I} + 2\eta\varepsilon'(\mathbf{v}) \tag{2}$$

where p is the pressure, $\mathbf{I}$ is the unit tensor, η is the viscosity and

$$\varepsilon'(\mathbf{v}) = \varepsilon(\mathbf{v}) - \frac{1}{3}(\nabla \cdot \mathbf{v})\mathbf{I} \tag{3}$$

is the deviatoric strain rate tensor. In Equation 3, $\varepsilon(\mathbf{v})$ is the total strain rate tensor, while the second term on the right-hand side is the divergence of the velocity field, that is, the rate at which the fluid volume changes at a point. There are different notations for the strain and the strain rate tensors, such as ε, $\dot{\varepsilon}$, $\varepsilon(\mathbf{u})$, $\varepsilon(\mathbf{v})$. Here we use ε as an

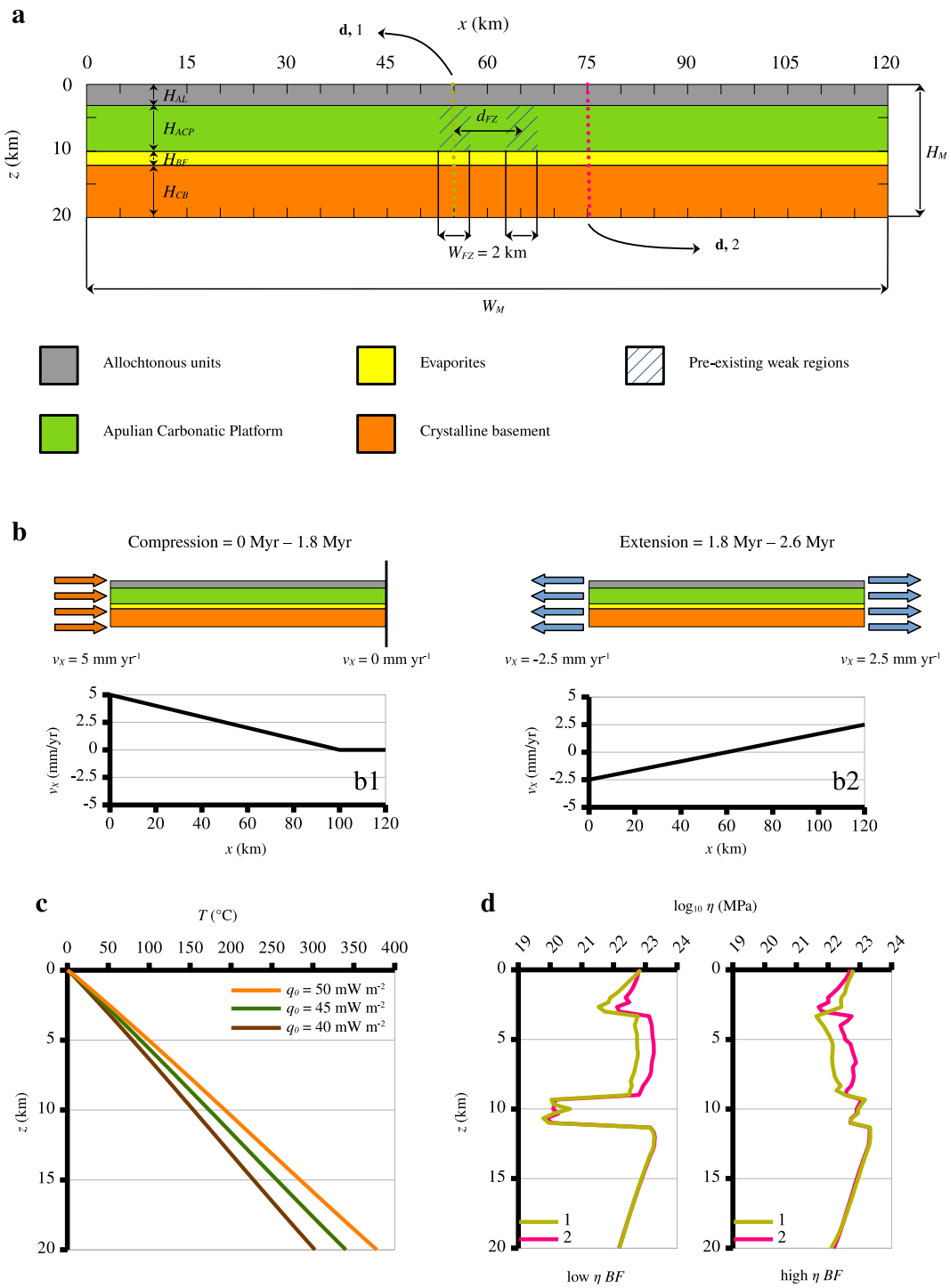

Figure 2. Model setup. (a) Lithological and structural layout. The hatched pattern regions in the ACP layer represent the preexisting weak structures. The dotted vertical lines indicate the strength profiles in panel (d), within (yellow line) and outside (magenta line) the faulted region. (b) Velocity boundary conditions. A first phase, lasting 1.8 Myr, is characterized by zero velocity at the right boundary and compressional velocity v_x^C at the left boundary, which is kept constant in the simulation for the entire phase and varies in our study between 3 and 7 mm yr^{-1}. In the second phase, lasting 0.8 Myr, the model incorporates a symmetric extensional velocity field, with $v_x^C = 2.5$ mm yr^{-1}. The diagrams show the values of v_x^C applied at the bottom boundary of the model during compression (b1) and extension (b2). (c) $T - z$ profiles for the model domain at the simulation onset. The geotherm has been calculated by imposing $q_0 = 40$ mW m^{-2} (brown line), 45 mW m^{-2} (green line), 50 mW m^{-2} (orange line). (d) $\eta - z$ profiles for the model domain at the simulation onset. The yellow line refers to profile 1 (within the fault region of the ACP, whereas the magenta line refers to profile 2 (outside the fault region of the ACP). The left panel refers to simulations where the BF has low values of η_{EFF}, whereas the right panel refers to simulations where the BF has high values of η_{EFF}.

Table 1
Model Parameters Common to All Simulations

Parameter name	Symbol	Measurement unit	Value
Model horizontal extension	W_M	km	120
Model vertical extension	H_M	km	20
Cell dimension	c_E	m	333
Free surface diffusion coefficient	ζ	$m^2\ s^{-1}$	$0–10^{-6}$
Simulated time	t	Myr	2.6
Compression:			
Duration	t_C	Myr	1.8
Left boundary velocity	v_x^A	$mm\ s^{-1}$	3-5-7
Right boundary velocity	v_x^B	$mm\ s^{-1}$	0
Extension:			
Duration	t_E	km	0.8
Left boundary velocity	v_x^A	$mm\ s^{-1}$	−2.5
Right boundary velocity	v_x^B	$mm\ s^{-1}$	2.5
Surface temperature	T_0	°C	0
Base model temperature	T_b	°C	302-340-378
Surface heat flow ($t = 0$)	q_0	$mW\ m^{-2}$	40-45-50
Weak regions in the ACP:			
Distance	d_{FZ}	km	2.5-5-7.5-10
Extension	W_{FZ}	km	2
Layer thickness:			
AU	H_{AU}	km	3
ACP	H_{ACP}	km	6
BF	H_{BF}	km	2
CB	H_{CB}	km	9

operator, meaning that, for the strain rate, it is not used on its own but it is applied to the velocity **v** field. Accordingly, $\varepsilon(\mathbf{v}) = \frac{1}{2}\left(\nabla\mathbf{v} + \nabla\mathbf{v}^T\right)$ is the strain rate tensor. Likewise, if $\mathbf{u}(\mathbf{x}, t)$ is the displacement field $\varepsilon(\mathbf{u}) = \frac{1}{2}\left(\nabla\mathbf{u} + \nabla\mathbf{u}^T\right)$ is the strain tensor. The square root second invariant of $\varepsilon(\mathbf{v})$, also defined as effective strain rate (e.g., Ranalli, 1995), is indicated by $\dot{\varepsilon}_{II} = \sqrt{\frac{1}{2}\left(\dot{\varepsilon}_{ii}\dot{\varepsilon}_{jj} - \dot{\varepsilon}_{ij}\dot{\varepsilon}_{ji}\right)}$.

For high-viscosity fluids, the inertial term in Equation 1 can be neglected as a consequence of the very small velocity variations in time and the Navier-Stokes equation, obtained from Equations 1–3, reduces to the Stokes equation of motion:

$$-\nabla \cdot 2\eta\varepsilon'(\mathbf{v}) + \nabla p = \rho\mathbf{g} \tag{4}$$

3.2.2. Mass Conservation

The conservation of mass is expressed by the continuity equation

$$\frac{\partial\rho}{\partial t} + \nabla \cdot (\rho\mathbf{v}) = 0 \tag{5}$$

meaning that the change in density over the time $\frac{\partial\rho}{\partial t}$ of a system must be compensated by a mass inflow or outflow given by the divergence of $\rho\mathbf{v}$.

Our model domain has a vertical extension of 20 km, therefore the difference in temperature T and pressure p between the top and the bottom boundaries are, respectively, less than 400°C (Figure 2c) and 600 MPa. This implies that the $p-T$-related density variations $\frac{\Delta\rho}{\rho_0}$ are less than 2%. Under this assumption, the terms $\frac{\partial\rho}{\partial t}$ and $\nabla\rho\cdot\mathbf{v}$ can be neglected in Equation 5, that reduces to

$$\nabla\cdot\mathbf{v}=0 \tag{6}$$

implying fluid incompressibility. Equation 3 in turn reduces to

$$\varepsilon'(\mathbf{v})=\varepsilon(\mathbf{v}) \tag{7}$$

Density variations disappear from Equation 4 and

$$\dot{\varepsilon}_{II}=\sqrt{\frac{1}{2}\dot{\varepsilon}_{ij}\dot{\varepsilon}_{ij}}. \tag{8}$$

3.2.3. Energy Conservation

Equations 4 and 6 are solved coupled with the heat equation

$$\rho C_p\left(\frac{\partial T}{\partial t}+\mathbf{v}\cdot\nabla T\right)=\nabla\cdot k\nabla T \tag{9}$$

where T is the temperature, C_p is the heat capacity and k is the thermal conductivity.

The meaning of Equation 9 is that the thermal energy change over time $\rho C_p\frac{\partial T}{\partial t}$ is primarily due to the mechanisms described by the following terms: the term on the left-hand side $\rho C_p\mathbf{v}\cdot\nabla T$ accounts for the advective heat transport, whereas the term in the right-hand side $\nabla\cdot k\nabla T$ accounts for the conductive heat transport. Due to the low heat production in sedimentary rocks (e.g., Hasterok et al., 2018), which constitute a great part of our model, and the decrease in radiogenic heat production with depth (e.g., Jaupart et al., 2016, and references therein), inner heat production due to the decay of radiogenic elements has been neglected.

3.2.4. Visco-Plastic Rheology and Brittle/Ductile Transition

At crustal depths and temperatures, the dominant mechanism of viscous deformation is dislocation creep. Therefore, viscosity η_{dis} is given by Billen and Hirth (2007)):

$$\eta_{dis}(x,z,t)=\frac{1}{2}D_r^{-\frac{1}{n}}\dot{\varepsilon}_{II}^{\frac{1-n}{n}}\exp\left(\frac{E}{nRT}\right) \tag{10}$$

where D_r is the Dorn parameter, n is the stress exponent of the Dorn equation, E is the activation energy and R is the gas constant. Accordingly, the effective stress $\Delta\sigma_M$, representing the crustal resistance to viscous deformation, is given by (e.g., Filippucci et al., 2019):

$$\Delta\sigma_M(x,z)=2\eta_{dis}\dot{\varepsilon}_{II}=D_r^{-\frac{1}{n}}\dot{\varepsilon}_{II}^{\frac{1}{n}}\exp\left(\frac{E}{nRT}\right) \tag{11}$$

To describe the evolution of faults, the plastic deformation limits $\Delta\sigma_M$ (e.g., Thieulot, 2011; Van Zelst et al., 2022) through the Drucker-Prager criterion, where the yield stress in 2D $\Delta\sigma_m$ is equivalent to the Mohr-Coulomb yield surface:

$$\Delta\sigma_m(x,z)=\sigma_y=(p\sin\phi+C\cos\phi) \tag{12}$$

where C is the cohesion factor and ϕ is the angle of friction. In this manner, we can define a "plastic" yield viscosity

$$\eta_y = \frac{\Delta\sigma_m}{2\dot{\varepsilon}_{II}} \tag{13}$$

and a crustal effective viscosity η_{eff}, which takes the minimum value between η_y and η_{dis}:

$$\eta_{eff}(x, z, t) = \min(\eta_y, \eta_{ds}) \tag{14}$$

Likewise, the effective differential stress for crustal deformation σ_{eff} is given by the minimum value between $\Delta\sigma_M$ and $\Delta\sigma_m$ (e.g., Filippucci et al., 2019; Gerya, 2019; Lavecchia et al., 2022)

$$\sigma_d(x, z) = \min[\Delta\sigma_M(x, z), \Delta\sigma_m(x, z)] \tag{15}$$

where $\sigma_d(x, z) = \Delta\sigma_m(x, z)$ the rheological behavior is brittle, while where $\sigma_d(x, z) = \Delta\sigma_M(x, z)$ the rheological behavior is ductile. The step function

$$Rh(x, z) = \begin{cases} 0 & \text{if} \quad \sigma_d = \Delta\sigma_M(x, z) \\ 1 & \text{if} \quad \sigma_d = \Delta\sigma_m(x, z) \end{cases} \tag{16}$$

represents by 0 and 1 the ductile and brittle behavior respectively.

3.2.5. Coulomb Stress and Fault Activation

At the end of our simulations, we observe that linear structures affect the model's plastic domains, where $\dot{\varepsilon}_{II}$ is higher than the adjacent regions. We interpret such structures as faults and pay particular attention to providing insight into their potential to generate earthquakes. For this purpose, we calculate the value of the components T_i of the Cauchy stress tensor $\boldsymbol{T}$ (e.g., Irgens, 2008) in each node composing our model's domain:

$$T_i = \sigma_{ij} n_j \tag{17}$$

where σ_{ij} are the stress components and n_j are the components of the unit vector orthogonal to the fault. Such product depends on the faults' dip angle $\varphi \simeq 2/3\,\pi$, which in our model is fairly constant. The $\boldsymbol{T}$ tensor components are used to calculate the normal σ_n and shear stresses τ along the faults:

$$\sigma_n = T_x \sin\varphi + T_y \cos\varphi \tag{18}$$

$$\tau = \sqrt{|\boldsymbol{T}|^2 - {\sigma_n}^2} \tag{19}$$

On the basis of the values of stress and rheology obtained in our simulations, we infer that seismic activity may potentially occur in plastic regions where the Coulomb stress $\sigma_C > 0$ (e.g., King et al., 1994; Tallarico et al., 2005):

$$\sigma_C = \tau - \tan(\phi)(\sigma_n - p_f) \tag{20}$$

where p_f is the pore fluid pressure. Regions where fluids are present ($p_f > 0$) are introduced in the model at the last time step of the simulation that better reproduces the geological and geophysical characteristics of the SE VA, therefore approximating the characteristics along the profile C-D (Figure 1) cross-cutting the PL and the CM2 seismic clusters (case C, see Sections 3.5 and 4.3). This allows us to consider the effect of the water load associated with the recent PL presence (e.g., Stabile, Giocoli, Perrone, et al., 2014; Stabile et al., 2015; Telesca et al., 2015) and the even more recent reinjection activity in the CM2 well (e.g., Rinaldi et al., 2020; Stabile, Giocoli, Lapenna, et al., 2014). The region where we introduce the presence of fluids related to the PL is circumscribed by the upper and lower limit of the ACP and the weak zones that cross-cut this layer (Figure 2), while fluids underneath the CM2 are introduced along a high $\dot{\varepsilon}_{II}$ structure in the ACP plastic domain, E of the easternmost weak zone within the ACP. The fluid reinjection pressure is known for the CM2, and has a value

$40.6 \leq p_f \leq 45.6$ MPa (Stabile, Giocoli, Lapenna, et al., 2014). Differently, in the PL region, p_f can be evaluated by considering the hydrostatic pressure of the water column h_w above the seismicity cluster in the proximity of the water reservoir. Since h_w is subjected to seasonal fluctuations within the order of ± 15 m (Stabile, Giocoli, Lapenna, et al., 2014; Stabile et al., 2015), p_f variations are negligible ($\Delta p_f < \pm 0.15$ MPa). Therefore, we have assumed that:

$$p_f = 0.4 \cdot p_{lith} + p_w = 0.4 \cdot \rho(z) g z + p_w \tag{21}$$

where $p_{lith} = \rho g z$ is the lithostatic pressure underneath the PL cluster and $p_w \simeq 0.4$ MPa, calculated by assuming that the depth of the lake has a constant value of 40 m.

3.3. Initial and Boundary Conditions

3.3.1. Initial Condition

Temperature is the only explicitly time-dependent quantity of the model for which it is necessary to set the initial condition. This is provided by a linear geotherm as follows:

$$T_i(z, t = 0) = T(z_n) + \frac{q_0(z_n)}{k_n}(z - z_n) \tag{22}$$

where z_n is the z coordinate of the ith layer, q_0 is the surface vertical heat flow at $t = 0$. The initial vertical heat flow is

$$q_i(z) = -k \frac{dT_i}{dz} \tag{23}$$

In Figure 2c, $T_i(z)$ is shown for different values of q_0.

3.3.2. Top

At the Earth's surface ($z = z_0$) we assume a constant temperature

$$T(z_0) = T_0 \tag{24}$$

and a free surface subjected to erosion/sedimentation, which is simulated by assuming lateral diffusion of the surface:

$$\frac{\partial h}{\partial t} = \zeta \frac{\partial^2 h}{\partial x^2} \tag{25}$$

where ζ is the hillslope diffusion coefficient (diffusivity), and $h(x)$ is the height of a point along the top boundary with respect to the unperturbed surface (Paola, 2000).

The vertical surface velocity

$$v_{z0}(x, z_0, t) = \frac{\partial h(x, t)}{\partial t} \tag{26}$$

is used to deform the surface and as a boundary condition to solve the Laplace equation and determine the mesh velocity in the domain interior. Diffusion is applied at every timestep, mimicking surface processes of erosion and deposition. In our simulations, $\zeta = 10^{-6}$ m^2 s^{-1}, causing maximum values of erosion $\simeq 2$ mm yr^{-1}.

3.3.3. Left and Right

The western Mediterranean area was dominated by the eastward migration of the Apennines arc during the Neogene and part of the Quaternary (Gueguen et al., 1998). This tectonic movement is taken into account

imposing a compressional horizontal velocity v_x^C at the left boundary $x = x_A$ for the first 1.8 Myr. In this time span, the horizontal velocity is kept to 0 at the right boundary $x = x_B$. For the remaining 0.8 Myr, a symmetric extensional velocity v_x^E, is imposed to reproduce the extensional tectonics that characterizes the VA at the present day (e.g., Cinque et al., 1993; D'Agostino et al., 2008; Serpelloni et al., 2005).

$$v_{xA}(x_A, z, t) = \begin{cases} v_x^C & \text{if } 0 \le t \le 1.8 \text{ Myr} \\ -v_x^E & \text{if } 1.8 < t \le 2.6 \text{ Myr} \end{cases} \tag{27}$$

$$v_{xB}(x_B, z, t) = \begin{cases} 0 & \text{if } 0 \le t \le 1.8 \text{ Myr} \\ v_x^E & \text{if } 1.8 < t \le 2.3 \text{ Myr} \end{cases} \tag{28}$$

The boundary conditions on temperature both at the right and the left boundary are given by Equation 22.

3.3.4. Bottom

At the bottom of the domain $z = z_b$ we assume:

- A constant temperature T_b given by Equation 22

$$T_b = T_i(z_b) \tag{29}$$

- A horizontal velocity v_{xb}^C during the compressional phase ($t \le 1.8$ Myr) which decreases linearly down to 0 when $x = 100$ km, corresponding to an approximate distance of the VA of 40 km from the Bradanic through. For the remaining part of the bottom boundary (100 km $\le x \le$ 120 km), v_{xb}^C is kept constant at 0.
- A horizontal velocity v_{xb}^E during the extensional phases ($t > 1.8$ Myr) that varies linearly from $v_{xb}^E = -2.5$ mm/yr when $x = 0$ to $v_{xb}^E = 2.5$ mm/yr when $v_{xb}^E = 120$ km.

3.4. Lithological and Structural Aspects

In the VA, several distinct formations and units have been recognized, with variable geometrical and lithological characteristics. In particular, the AU overlying the carbonate formations of the ACP show distinctive lithological and structural complexities (Dell'Aversana, 2003; Mazzoli et al., 2013; Menardi Noguera & Rea, 2000; Shiner, Mazzoli, & Cello, 2004). The lithologies occurring in the VA region have been approximated by four layers, with a tabular shape at the simulation onset (Figure 2a) and distinct physical/rheological features. The parameters adopted for each layer are given in Table 2. These layers, from top to bottom, are: (a) AU, (b) ACP, (c) BF, (d) CB.

The rheological parameters have been calculated for each layer, taking into account the presence of different mineralogical phases and their relative volume percentages and following the averaging method proposed by Ji et al. (2003). The compositions for each lithology are shown in Table 3.

The presence of inherited structures controlling the localization of the contractional and extensional structures in the ACP (Shiner, Mazzoli, & Cello, 2004; Valoroso et al., 2011) has been taken into account by assuming the presence of weak zones in the ACP (Figure 2a), characterized by low values of C, and ϕ as reported in Table 2. These weak zones retain the low values of plastic rheological parameters for the entire simulation time and are treated as distinct compositional fields within ASPECT, therefore deforming coherently with the other lithologies implemented in the model (Figures 2–4 and 8).

3.5. Parameters Sensitivity Analysis and Reference Configuration

In order to test which parameter(s) affect our model's results and produce a better correspondence with the geological/geophysical observables and the seismological characteristics in the VA, we have carried out a set of 24 simulations, with different choices of the following parameters (Table 4):

1. Distance of the inherited fault zones within the ACP (d_{FZ}, cases A, B, C, D)
   Although the role of pre-existing faults in the geodynamic evolution of the VA has already been acknowledged

Table 2
Parameters Adopted in Each Layer

Parameter name	Symbol and measurement unit	AU	ACP (faults)	ACP	BF	CB
Thermal conductivity	k, W m^{-1} K^{-1}	2.4	2.7	2.7	2.7	2.7
Density	ρ, kg m^{-3}	2,400	2,600	2,600	2,700	2,800
Heat capacity	C_p, J kg^{-1} K^{-1}	878	900	900	900	900
Dorn parameter	D, Pa^{-n} s^{-1}	4.59×10^{-48}	1.31×10^{-21}	1.31×10^{-21}	1.5×10^{-24}	1.27×10^{-34}
Stress exponent	n	6.98	3.15	3.15	3	5.13
Activation energy	Q, kJ mol^{-1}	134	167.5	167.5	75–145	254
Cohesion	C, MPa	75	75	20	75	75
Angle of friction	ϕ, °	33	33	10	33	33

(e.g., Valoroso et al., 2011), there is no information on the mutual distance d_{FZ} between these faults at the beginning of Quaternary, and how the tectonic structure of the region is affected by this parameter. Therefore, we have carried out 4 simulations where d_{FZ} is, respectively, 2.5, 5, 7.5, and 10 km. We have assumed d_{FZ} reference values = 5 and 7.5 km. Consequently, all the following sensitivity analyses have been carried out with both these values.

2. Surface heat flow at the beginning of the simulation ($q_{0,s}$, cases E, F, G, H)
   The regional value of heat flow in the Apennines region between 40 and 50 mW m^{-2} reflects the geotherm that characterizes the VA (Figure 2c, see 22) and, consequently, the basin's viscosity profile (see Equation 10), particularly at the simulation onset. We have imposed $q_{0,s}$ = 50 mW m^{-2} in the entire model domain as our reference value, but we tested the impact of the initial geotherm on the mechanical characteristics of the crust, by giving $q_{0,s}$ the values 40 and 45 mW m^{-2}.
3. Compressional velocity (v_x^C, cases I, J, K, L)
   The compressional velocity v_x^C has not been precisely quantified but can be estimated within the order of a few mm yr^{-1} (Gueguen et al., 1998; Maschio et al., 2005). Variations of v_x^C have an impact on the pre-extensional structure of the VA region and its topography, with subsequent effects on both the lithostatic and dynamic pressure in the valley. Therefore, we tested variations of v_x^C during the compressional phase of our simulations, by assuming a reference value $v_x^C = 5$ mm yr^{-1} and giving this parameter alternative values of 3 and 7 mm yr^{-1}.
4. Effect of erosion (ζ, cases M, N, O)
   Several studies highlight the impact of surface processes on the evolution of geodynamically active areas (e.g., Sternai et al., 2021), therefore we evaluated the effects of erosion and sedimentation on the VA by running simulations where $\zeta = 0$, and therefore surface processes are not implemented, or when $\zeta = 10^{-8}$, to observe the effect of slow erosion/deposition rates on the VA basin's opening and expansion.
5. Lateral variations of η in the BF (cases P, Q, R, S, T, U)
   Although there is a general consensus on the lithologies that make up the tectonic units in the VA, their mineral composition might be extremely variable. In particular, the BF can have a key role in the tectonic evolution of the region, since it represents a rheological boundary between the Sedimentary Cover (SC) and the CB and may produce different tectonic styles in these two crustal layers. For the BF, we have varied the parameter E in Equations 3 and 10, and therefore η_{EFF}, to consider either a layer fully composed of carbonates, or characterized by a high gypsum content. We tested the effect of these variations on the VA present-day tectonic setting by considering three configurations at the simulation onset (Figure 2d):
   - $\eta_{EFF} \simeq 10^{20}$ Pa s,
   - $\eta_{EFF} \simeq 10^{20}$ Pa s if $x < 60$ km and $\eta_{EFF} \simeq 10^{22}$ Pa s if $x > 60$ km,
   - $\eta_{EFF} \simeq 10^{22}$ Pa s if $x < 60$ km and $\eta_{EFF} \simeq 10^{20}$ Pa s if $x > 60$ km,
6. Presence or absence of inherited faults in the ACP (ϕ, C) (cases V, W)
   To evaluate the effect of inherited structures on the final tectonic configuration of the VA, and especially on the development of the Eastern Agri Fault System and the Mts. Maddalena Fault System, we carried out simulations where fault zones in the ACP are absent or there is only one preexisting fault.

Table 3
Composition and Volume Fraction of Minerals Composing Each Layer

Layer	CC	Dm	Ab	An	Qz	Ph	Gt	Py
AU	20	10	10	0	20	40	0	0
ACP	50	50	0	0	0	0	0	0
BF	0	100	0	0	0	0	0	0
CB	0	0	25	7	25	15	14	14

Note. Cc = calcite; Dm = dolomite; Ab = albite; An = anorthite; Qz = quartz; Ph = phyllosilicates; Gt = garnet; Py = pyroxene.

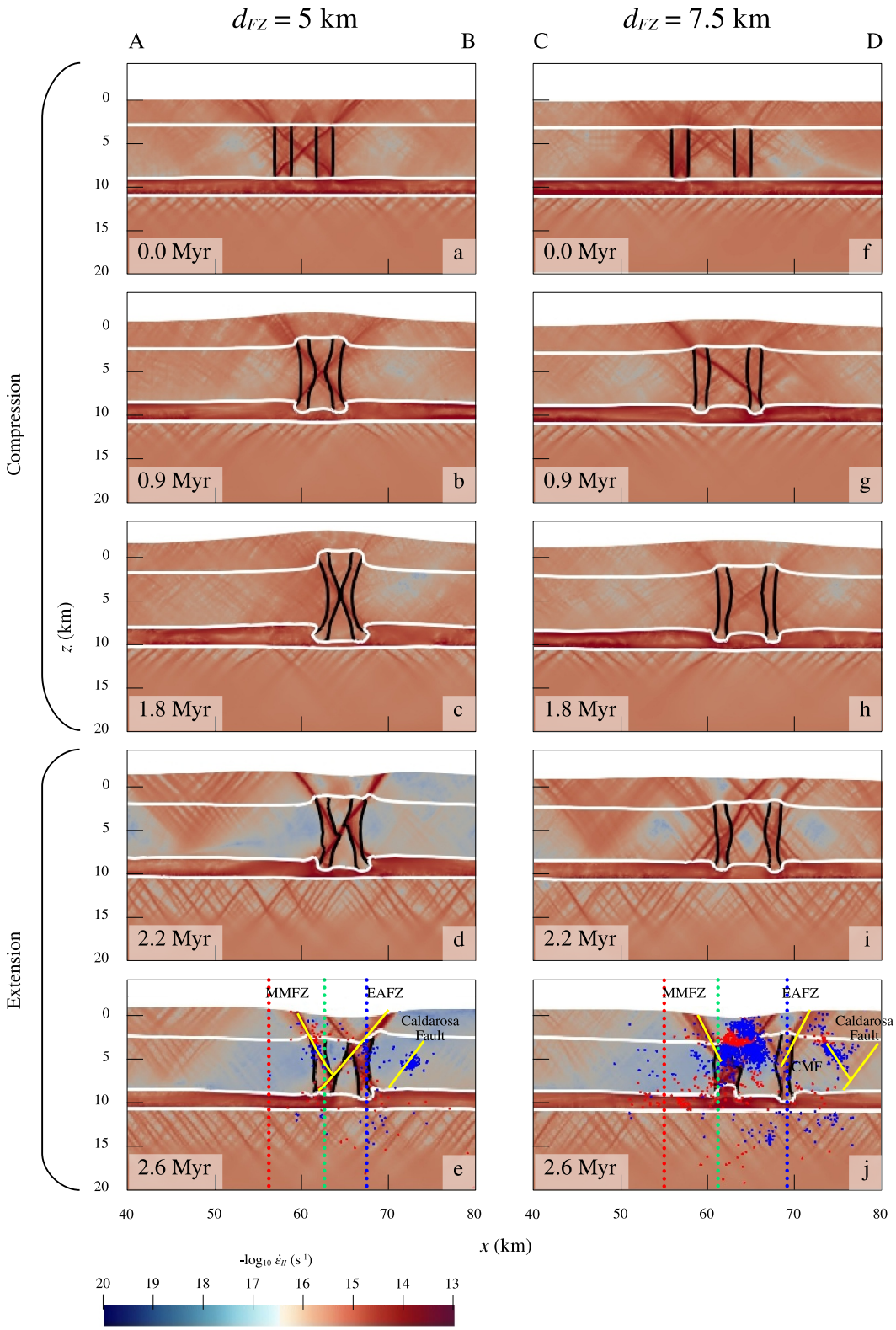

Figure 3.

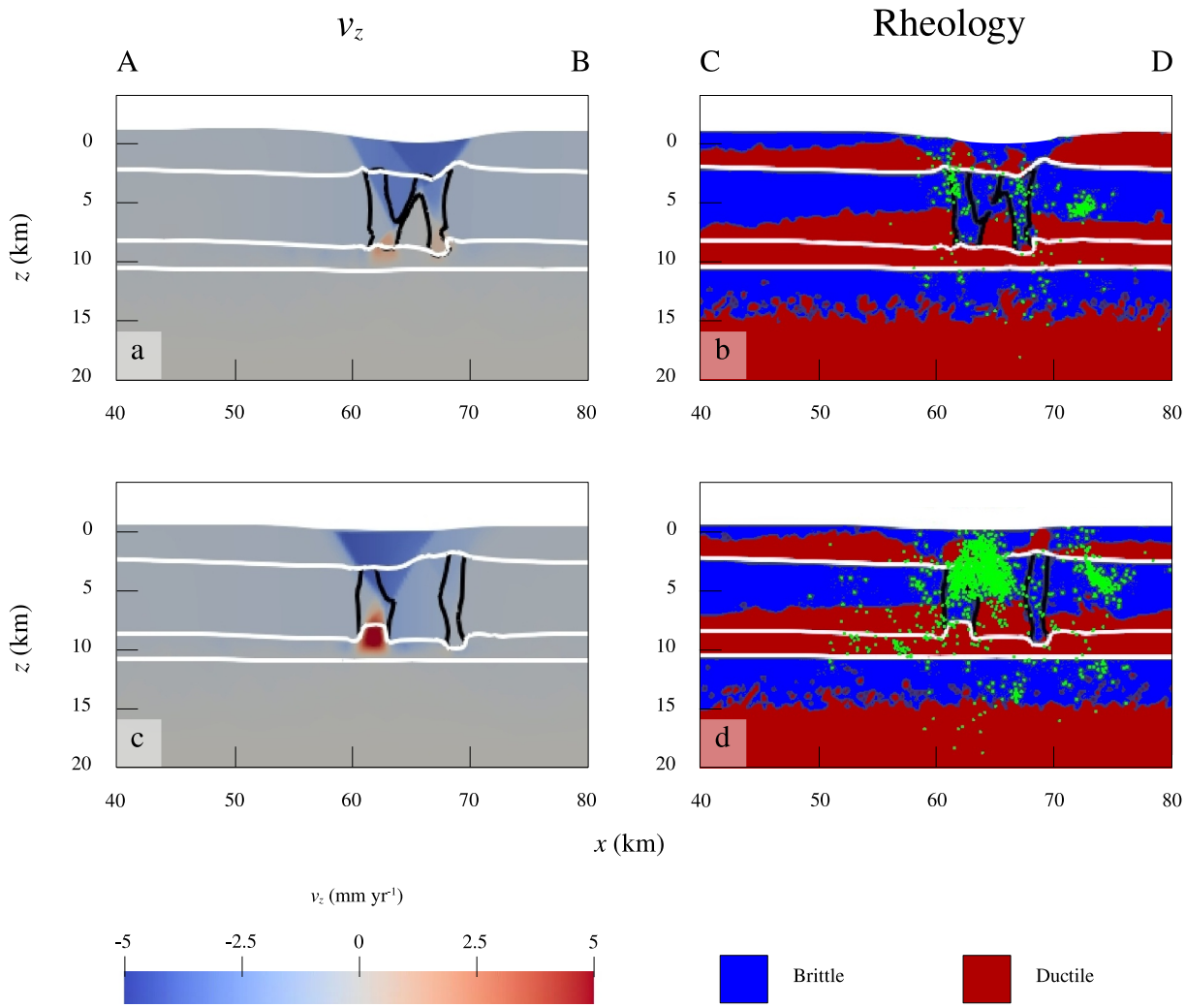

Figure 4. v_z distribution and rheological behavior for case B (panels a and b) and case C (panels c and d). The green dots indicate the position of the hypocenters, respectively, in the NW (panel b) and SE (panel c) VA region. The white lines indicate the lithological boundaries, whereas the black lines indicate the boundaries of the weak zones within the ACP.

7. Extension confined in the sedimentary cover (cases X, Y)
   We have tested the possibility that the extensional deformation is mainly due to the collapse of the Apennines chain. In this case, the horizontal velocity v_x^E is applied to the sedimentary cover, whereas we imposed a velocity $v_x^E = 0$ at the left and right boundaries of the basement.
8. Width of the fault zones (cases Z, AA, AB)
   The thickness of the rock intervals subjected to fracturing and faulting can vary between thin intervals of fractured rocks to large regions where rocks lose their cohesion. We have taken it into account by varying d_{FZ} between 1 and 4 km. In addition, we have tested the possibility that the VA overlies an extended region of intensely fractured carbonates of the ACP, by including a single faulted region with $d_{FZ} = 8$ km.

Figure 3. $\dot{\varepsilon}_{II}$ distribution evolution for our reference simulations B ($d_{FZ} = 5$ km, panels a–e) and C ($d_{FZ} = 7.5$ km, panels f–j). The blue dots in panels (e) and (j) indicate the locations of the hypocenters that fall in the model's brittle domain, whereas the red dots in the same panels indicate the locations of the hypocenters that fall in the model's ductile domain (see Figure 4). The dotted lines in panel (e) indicate the vertical profiles shown in Figure 5, whereas the dotted lines in panel (j) indicate the vertical profiles shown in Figure 6, with the colors of the lines matching the colors of the plots. The yellow lines indicate the known faults identified in our model. The white lines indicate the lithological boundaries, whereas the black lines indicate the boundaries of the weak zones within the ACP.

Table 4
Simulation Suite for the Study of Parameter Sensitivity

Case study	d_{FZ} (km)	q_0 (mW m^{-2})	v_x^C(mm yr^{-1})	ζ (m^2 s^{-1})	η_{EFF} (Pa dss)	Nr. faults (thickness)	Applied v_x^E
A	2.5	50	5	10^{-6}	10^{20}	2 (2 km)	All lateral boundaries
B*	5	50	5	10^{-6}	10^{20}	2 (2 km)	All lateral boundaries
C*	7.5	50	5	10^{-6}	10^{20}	2 (2 km)	All lateral boundaries
D	10	50	5	10^{-6}	10^{20}	2 (2 km)	All lateral boundaries
E	5	45	5	10^{-6}	10^{20}	2 (2 km)	All lateral boundaries
F	5	40	5	10^{-6}	10^{20}	2 (2 km)	All lateral boundaries
G	7.5	45	5	10^{-6}	10^{20}	2 (2 km)	All lateral boundaries
H	7.5	40	5	10^{-6}	10^{20}	2 (2 km)	All lateral boundaries
I	5	50	3	10^{-6}	10^{20}	2 (2 km)	All lateral boundaries
J	5	50	7	10^{-6}	10^{20}	2 (2 km)	All lateral boundaries
K	7.5	50	3	10^{-6}	10^{20}	2 (2 km)	All lateral boundaries
L	7.5	50	7	10^{-6}	10^{20}	2 (2 km)	All lateral boundaries
M	5	50	5	0	10^{20}	2 (2 km)	All lateral boundaries
N	7.5	50	5	0	10^{20}	2 (2 km)	All lateral boundaries
O	5	50	5	10^{-8}	10^{20}	2 (2 km)	All lateral boundaries
P	5	50	5	10^{-6}	10^{22}	2 (2 km)	All lateral boundaries
Q	5	50	5	10^{-6}	10^{22} ($x < 60$ km)	2 (2 km)	All lateral boundaries
R	5	50	5	10^{-6}	10^{22} ($x > 60$ km)	2 (2 km)	All lateral boundaries
S	7.5	50	5	10^{-6}	10^{22}	2 (2 km)	All lateral boundaries
T	7.5	50	5	10^{-6}	10^{22} ($x < 60$ km)	2 (2 km)	All lateral boundaries
U	7.5	50	5	10^{-6}	10^{22} ($x > 60$ km)	2 (2 km)	All lateral boundaries
V	–	50	5	10^{-6}	10^{20}	1 (2 km)	All lateral boundaries
W	–	50	5	10^{-6}	10^{20}	0	All lateral boundaries
X	5	50	5	10^{-6}	10^{20}	2 (2 km)	Only SC
Y	7.5	50	5	10^{-6}	10^{20}	2 (2 km)	Only SC
Z	5	50	5	10^{-6}	10^{20}	2 (1 km)	All lateral boundaries
AA	5	50	5	10^{-6}	10^{20}	2 (4 km)	All lateral boundaries
AB	–	50	5	10^{-6}	10^{20}	1 (8 km)	All lateral boundaries

Note. The reference cases are indicated with *. See Sections 3.5 and 4.4 for further explanation.

Based on the geological constraints and the comparison between the results of our simulations and the geological and geophysical data available in the VA region Figure 7, we have taken as reference models the ones with the following implemented values:

- 2 preexisting faults in the ACP at the simulation onset,
- $d_{FZ} = 5$ km, 7.5 km (cases B and C, respectively),
- $q_{0,s} = 50$ mW m^{-2},
- $v_x^C = 5$ mm yr^{-1},
- $\zeta = 10^{-6}$ m^2 s^{-1},
- $\eta_{EFF} \simeq 10^{20}$ Pa s in the BF at the simulation onset.

More specifically, we consider case B as representative of the NW VA (profile A-B in Figure 1) and case C as representative of the SE VA (profile C-D in Figure 1, see Section 4).

4. Results

4.1. Tectonic Evolution

Our results are shown in Figures 3–8. They point out that the distance between faults d_{FZ} and the variations of viscosity η_{EFF} are the two parameters of greater impact for the tectonic setting and, therefore, for the seismicity distribution across the VA and neighboring regions. We have observed that variations of d_F are accompanied by significant differences in the evolution pattern of the structures appearing in the VA and their distribution, including the basin-bounding faults and the more external Costa Molina Fault (CMF) and Caldarosa Fault. This can be already noticed in our reference models when d_{FZ} varies between 5 and 7.5 km. Another primary aspect to consider is η_{EFF} in the BF. When this layer has low η_{EFF}, it serves as a décollement layer for the SC and causes an almost complete tectonic decoupling from the CB.

When $d_{FZ} = 5$ km (case B, Figures 3a–3e), we distinguish two main fault systems characterized by high $\dot{\varepsilon}_{II}$, that develop during the contractional phase from the preexisting weak zones in the ACP, and cross-cut both the carbonate formation and the overlying AU. This phase is characterized by the even distribution of $\dot{\varepsilon}_{II}$ between these two fault systems and persists for 1.2 Myr of simulated time. Subsequently, the SW fault system becomes dominant and assumes a listric geometry, whereas the NE fault system becomes antithetic and shows slightly lower $\dot{\varepsilon}_{II}$ values. These two fault systems circumscribe a <10 km wide region subjected to uplifting, with $v_z \simeq 3$ mm yr^{-1}. Compression acts on both the sedimentary cover and the basement, but the two layers show distinct deformation patterns, with a clear boundary represented by the BF. During the extensional phase, the region previously subjected to uplifting becomes a subsiding basin. Subsidence is caused by the development of both the SW and the NE border fault systems, with several active structures outlined by higher $\dot{\varepsilon}_{II}$ values, showing an initial symmetric configuration. Subsequently, similarly to the contractional phase, one of the two fault systems becomes dominant, with NE border faults cross-cutting the SW structures. In this phase, our model predicts the development of a series of synthetic and antithetic faults within the basin, that persist until the end of the simulation. This fault geometry is similar to what is observed today in the VA (Hager et al., 2021). The subsidence in the central region of the model occurs at a velocity $v_z < 5$ mm yr^{-1}, with values increasing NE-wards (Figures 4a and 5d). The resulting topography at the end of the simulation (Figure 5a) is characterized by a basin with a width ≃10 km, surrounded by reliefs with a height between 1,000 and 1,200 m. The final topographic profile, the mutual distance of the main fault systems developed in our model, and their locations with respect to the topography at the end of the simulation, are comparable with what is observed today in the NW VA (Figure 1). Therefore, we interpret the basin at the center of our model domain as the NW sector of the VA, surrounded by the Mts. Maddalena Fault System and the Eastern Agri Fault System.

When d_{FZ} is increased to 7.5 km (case C, Figures 3f–3j), we do not observe the evolution of one of the border faults into a listric fault during compression, but rather the development of two high-angle fault systems, with slightly lower dip angles when the border faults cross-cut the AU, and slightly higher angles when the border faults cross-cut the ACP. In addition, this simulation shows that the VA basin is characterized by several faults between the Mts. Maddalena Fault System and the Eastern Agri Fault System, coherently with previous studies in the region (Hager et al., 2021). At the end of the simulation, the distance between the border fault systems at the surface is ≃12 km (Figure 3), similar to what is observed today in the SE segment of the VA (Figure 1). The subsidence in the central region of the model occurs at a velocity comparable with the one observed in case B, but differently from this simulation, v_z values increase SW-wards (Figures 4c and 6d). The topographic profile of the region is also similar to what observed today in the SE VA (Figure 6a) and consists of a basin with a height ≃450 m a.s.l., surrounded by reliefs with heights between 1,000 m and 1,250 m. Therefore, given the characteristics of the border faults and the topographic profile obtained in this simulation, we interpret the results of case C as a reconstruction of the SE VA basin and surrounding regions until the present day.

A key aspect to analyze during the evolution of the VA and the surrounding regions, is the $\dot{\varepsilon}_{II}$ distribution between the AU and the ACP. More specifically, we have observed slightly higher values of $\dot{\varepsilon}_{II}$ at the base of the AU with respect to the ACP (Figures 5f and 6f), and different angles of the active structures, especially in the contractional phase, with lower angles within the AU (Figure 3). In agreement with this different $\dot{\varepsilon}_{II}$ distribution, we observe variations in the rheological behavior of the sedimentary cover (Figures 4b, 4d, 5g, 5j, 5m, 6g, 6j, and 6m), with a ductile layer constituted by the base of the AU, also characterized by low η_{EFF}, sandwiched between the stronger brittle top AU and ACP (Figures 5e, 5h, 5k, 6e, 6h, and 6k). Consequently, the base of the AU may constitute a décollement layer acting on a local scale. The presence of this ductile layer, however, is not observed in the areas

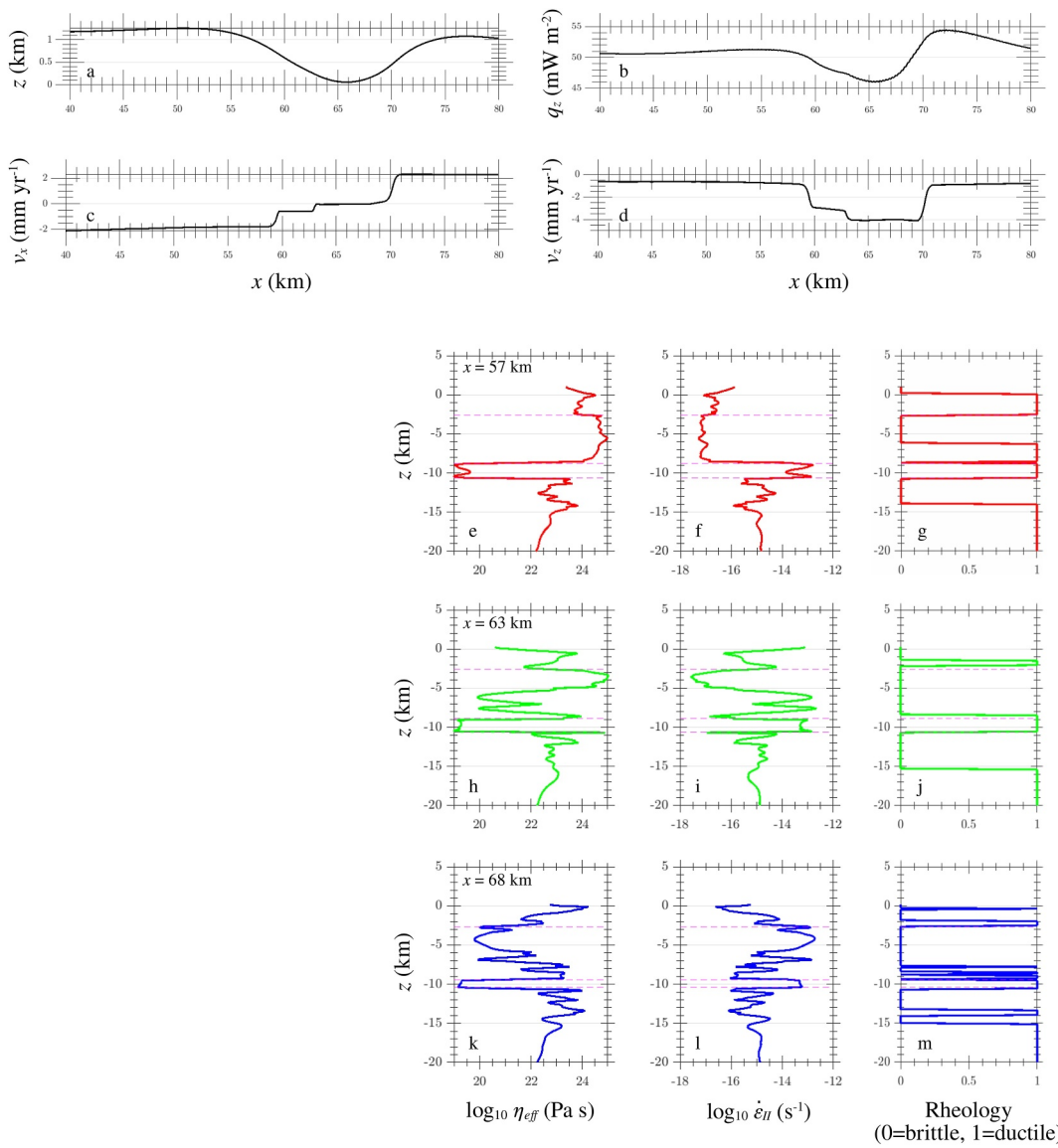

Figure 5. Horizontal and vertical plots for case B. The values of (a) z, (b) q_z, (c) v_x, and (d) v_z are taken at the top boundary. The measurement locations for the vertical plots of (e), (h), and (k) $\log_{10}\eta_{EFF}$, (f), (i), and (l) $\log_{10}\dot{\varepsilon}_{II}$, (g), (j), and (m) rheological behavior are specified in panels (e), (h), and (k) and are indicated by the colors of the plots, as shown in Figure 3.

surrounding the Eastern Agri Fault System and the Mts. Maddalena Fault System (Figures 4b and 4d), where the ACP is also characterized by low values of η_{EFF} (Figures 5e, 5h, 5k, 6e, 6h, and 6k) and high values of $\dot{\varepsilon}_{II}$ (Figures 5f, 5i, 5l, 6f, 6i, and 6l). In these areas, the preexisting fault zones within the ACP cause an increase in η_{EFF} around them, favoring a brittle behavior of the overlying units. As a consequence, our model predicts that the VA border fault zones are not confined within the AU, but in the absence of another shallower décollement level, they are rooted within the carbonate units, down to the BF.

As we can observe from the topographic profiles developed in cases B and C (Figures 5a and 6a), d_{FZ} does not seem to have a major effect on the final characteristics of the VA and the reliefs that surround the basin. In both cases, the VA has an approximate extension of 10–12 km, with the depocenter located at ≃65 km of our profile. Also, v_x does not show remarkable differences between the two cases (Figures 5c and 6c), with a stepwise increase NE-ward that highlights a fault-controlled extension of the VA. Differently, d_{FZ} has a remarkable effect on the subsidence pattern of the basin. The subsidence of the VA occurs via the vertical movement of blocks bounded by

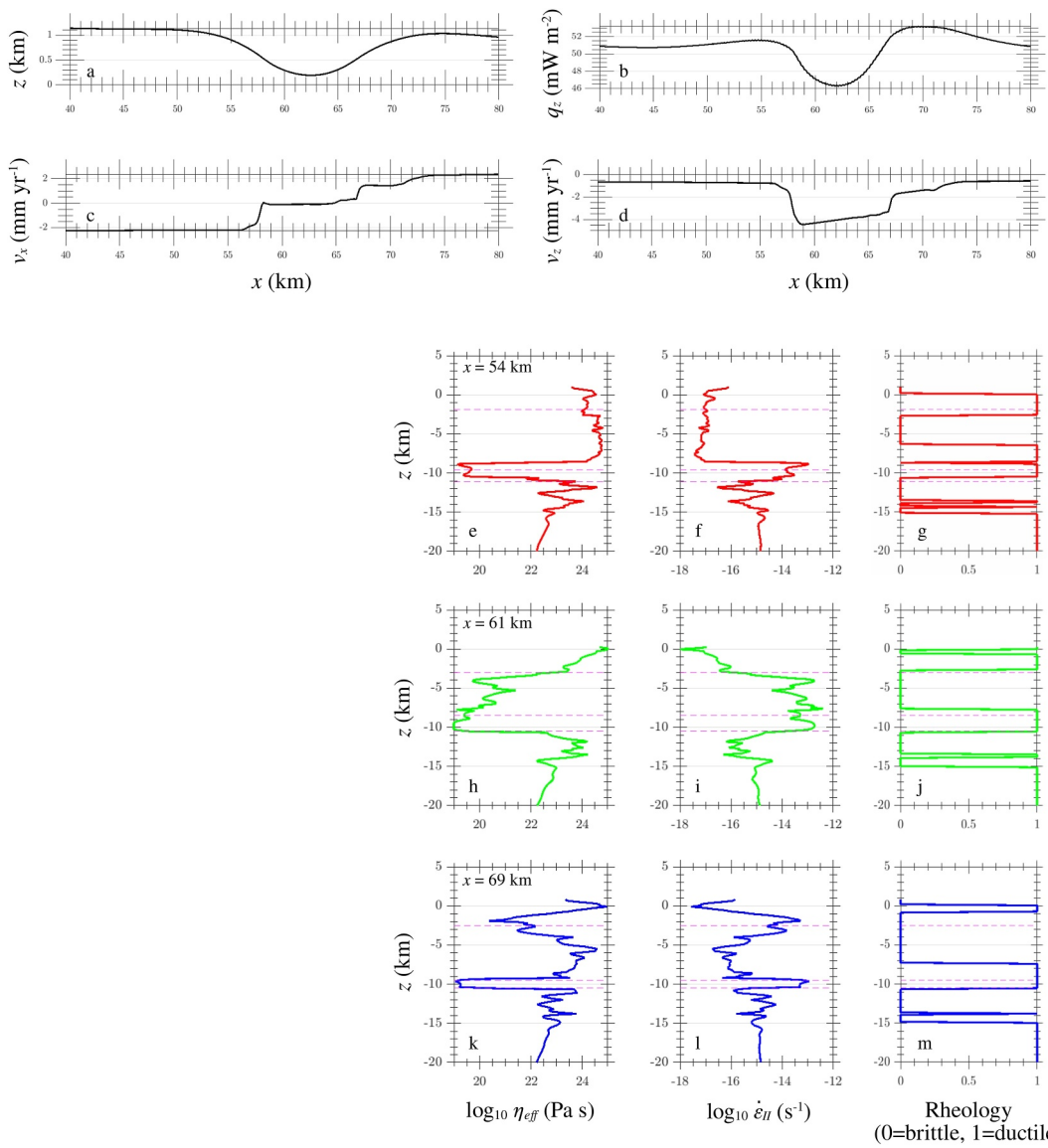

Figure 6. Horizontal and vertical plots for case C. The values of (a) z, (b) q_z, (c) v_x, and (d) v_z are taken at the top boundary. The measurement locations for the vertical plots of (e), (h), and (k) $\log_{10}\eta_{EFF}$, (f), (i), and (l) $\log_{10}\dot{\varepsilon}_{II}$, (g), (j), and (m) rheological behavior are specified in panels (e), (h), and (k) and are indicated by the colors of the plots, as shown in Figure 3.

faults cross-cutting both the AU and ACP, whereas the BF is only marginally affected (Figures 4a and 4c). In our reference simulations, we observe that v_z is maximum next to the Eastern Agri Fault System when $d_{FZ} = 5$ km (Figure 5d), and next to the Mts. Maddalena Fault System when $d_{FZ} = 7.5$ km (Figure 6d). This not only has an impact on the depocenter location within the VA, but highlights the presence of a series of active faults with seismogenic potential within the basin (see Section 4.3).

4.2. Surface Heat Flow, Velocity and Strain Rate

The validity of our interpretations has been verified by comparing the obtained values of q_z, $\dot{\varepsilon}_{II}$, $\mathbf{v}$ at the top boundary of our model with the observed values of these quantities. Results are summarized in Figures 7a and 7b. In addition, we have validated the tectonic setting of VA and surrounding regions obtained at the end of the model by comparing it with the locations of the earthquake hypocenters that characterize the region (see Section 4.3).

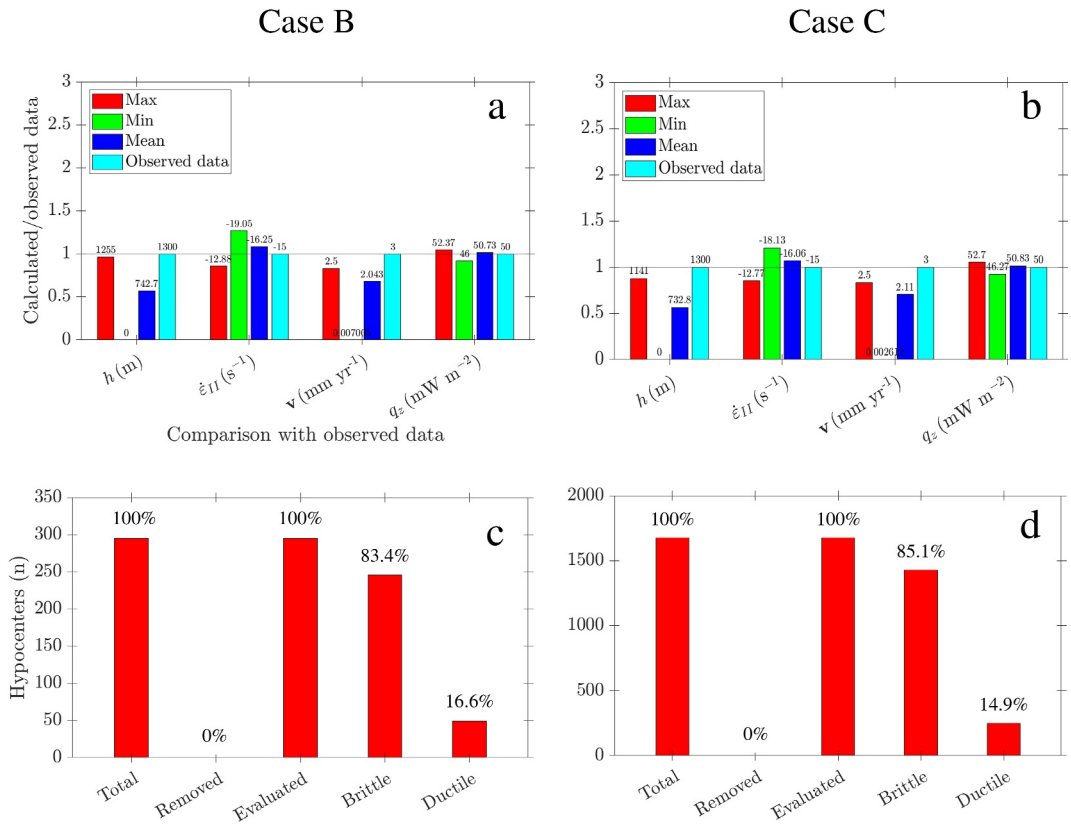

Figure 7. (a and b) Comparison between the values predicted by our models in case B (panel a) and C (panel b) for the topography, $\dot{\varepsilon}_{II}$, **v** and q_z on the model's top surface and the average value observed in the region. (c and d) Analysis of the earthquake hypocenters' location with respect to the brittle and ductile domains predicted by our models in case B (panel c) and in case C (panel d).

- The Basilicata region is characterized by average to low values of q_z. More in detail, with the exception of a small area NE of the VA with $q_z > 80$ mW m^{-2} (Figure 1), the commonly measured q_z values do not exceed 60 mW m^{-2} (Cataldi et al., 1995), with values around 50 mW m^{-2} (Scrocca et al., 2003) and 45 mW m^{-2} in the VA basin itself (e.g., Megna et al., 2014, and references therein). Our reference simulations predict values of q_z above 50 mW m^{-2} on the topographic reliefs surrounding the VA (Figures 5b and 6b). More specifically, the maximum output q_z value at the end of our simulations is ≃54 mW m^{-2} and is reached NE of the VA, whereas the minimum value is slightly higher than 46 mW m^{-2}, in the basin itself, in agreement with the studies mentioned above.
- The southern Apennines are characterized by NE-SW extension (e.g., Palano et al., 2011, and references therein), with average values of ≃3 mm yr^{-1} (e.g., D'Agostino, 2014). Tectonic extension, based on GPS data, and values of strain rate of ≃70 nstrain yr^{-1} (Palano et al., 2011; Silverii et al., 2016), correspond to ≃10^{-15} s^{-1}. In our model, we observe that both the superficial values of v_x (Figures 5c and 6c) and $\dot{\varepsilon}_{II}$ (Figure 3) are coherent with data measured in the previous surveys. Locally, our model shows higher $\dot{\varepsilon}_{II}$ values which are, however, confined to the active structures bordering the VA and do not weaken the reliability of our results.

4.3. Seismicity

An important test to validate the accuracy of our assumptions and the quality of our results is the comparison between the location of 2060 hypocenters of the VA seismicity from 2001 to 2019, the position of the main faults and the rheological domains predicted by our model for the units and formations composing the VA crust (Figures 3, 4, 7c, 7d, and 8). The seismicity catalog was compiled by merging the seismic catalogs documented in

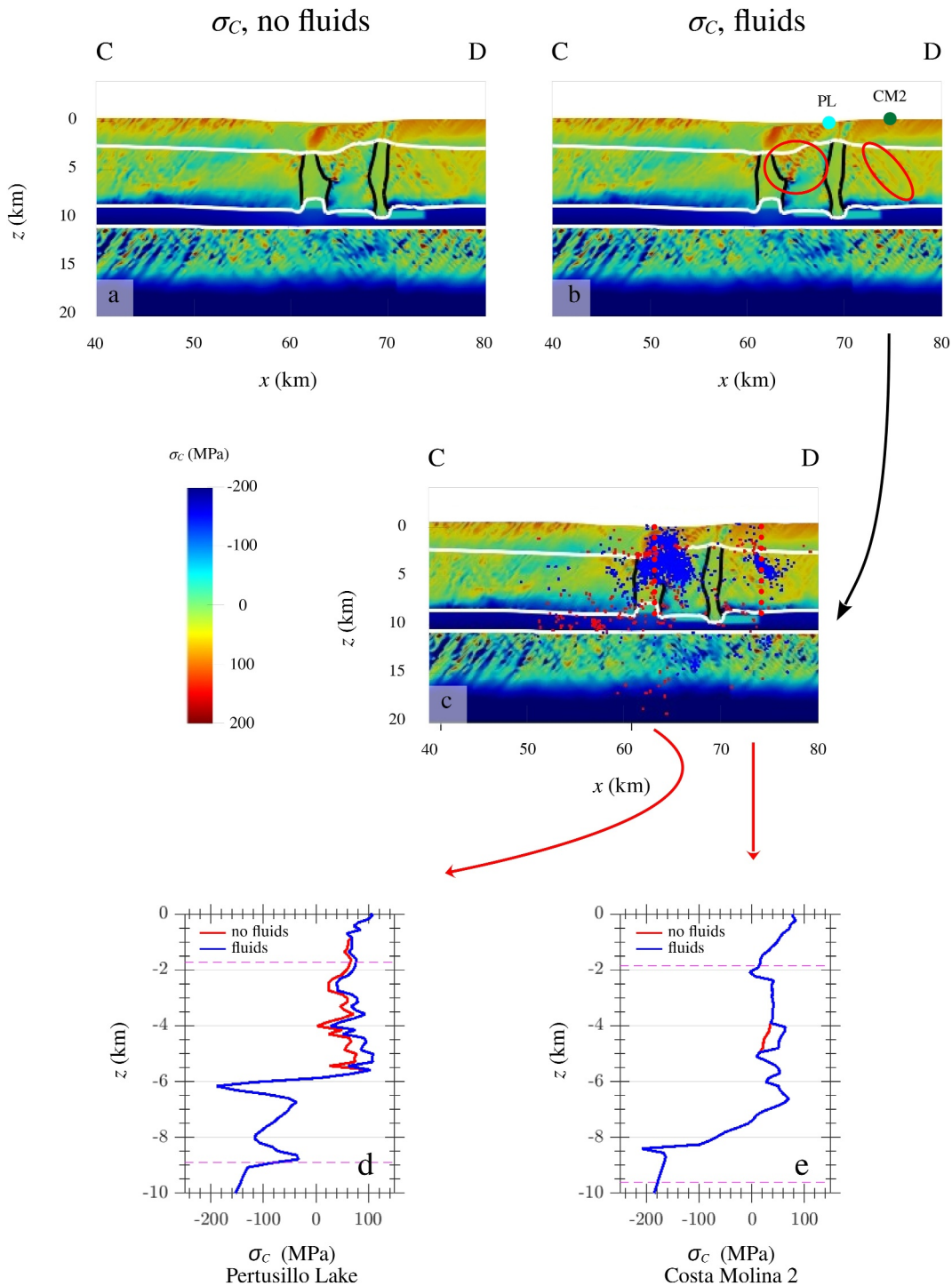

Figure 8. (a) σ_C values distribution for case C, when $p_f = 0$ in the entire domain. (b and c) σ_C values distribution for case C, when the known values of p_f are implemented in the model (see text for further details). In panel (b), the regions on the model circled in red (panel b) are the regions where the presence of fluids is detected. The light blue and dark green dots indicate the location of the PL and the CM2 reinjection well. In panel (c), the light blue dotted lines indicate the locations of the plots in panels (d) and (e). The dark blue dots indicate the locations of the hypocenters that fall in the brittle domain of our model, whereas the red dots indicate the locations of the hypocenters that fall in the ductile domain of our model. (d and e) $\sigma_C - z$ crustal profiles cross-cutting the PL (panel d) and CM2 (panel e) clusters. The red line indicates profiles where p_f is not implemented in the model, whereas the blue line indicates profiles where p_f is implemented.

Serlenga and Stabile (2019), Stabile et al. (2021), and Balasco et al. (2021). Only events within the dashed box of Figure 1 were considered in this study. The selected catalog of our interest is available in Lavecchia et al. (2024).

For case C, we verify that around 85% of the hypocenters fall in regions of the model with brittle behavior (Figure 7d), showing the very good quality of our assumptions for the lithologies, the geothermal characteristics, and the rheological parameters adopted in our simulations. This is evident not only in the sedimentary cover, where most earthquakes are located in the brittle ACP between 2 and 6 km, but also in the crystalline basement, where hypocenters are mostly located between ≃11 km (BF-basement boundary) and ≃15 km (brittle-ductile transition, Figures 4b and 4d). One example is the microearthquake sequence that recently occurred at those depths, located W-SW of Mt. Raparo near the Castelsaraceno village (Panebianco et al., 2023). We notice that most earthquakes that do not fall in the brittle field occur within the BF or next to this layer. However, the BF is a formation characterized by high lithological and thickness heterogeneity. Therefore, we can hypothesize that thicker intervals, or regions with higher dolomite %vol., may occur in our study area. The heterogeneity of the BF is probably the cause for the slightly less accurate prediction for case B, with around 83% of the hypocenters falling in regions of the model with brittle behavior (Figure 7c) since we observe that most hypocenters in ductile layers are located in this formation. In particular, a few earthquakes at a depth of ≃10 km seem to be located on the possible termination of the Eastern Agri Fault System within the BF. On the other hand, we observe a very good match between the hypocenters located in brittle areas and the location of the main faults predicted by our model. Therefore, we suggest that case B is also a reliable model of the NW sector of the VA.

Seismic activity that characterizes the SW sector of the VA is mostly concentrated at a depth between 2 and 6 km, with the clear appearance of two main clusters within the ACP (Figure 8). One of these clusters is located between the Eastern Agri Fault System and the Mts. Maddalena Fault System and is associated with the load of water from the Pertusillo Lake (e.g., Stabile, Giocoli, Lapenna, et al., 2014; Valoroso et al., 2009), whereas the other is located east of the Eastern Agri Fault System and is connected with the reinjection of wastewater from extraction activity in the CM2 well (Buttinelli et al., 2016; Improta et al., 2017; Stabile, Giocoli, Perrone, et al., 2014; Stabile et al., 2021). Seismic activity also occurs at a very shallow depth ($z < 2$ km) in an area located between the VA border faults, and in a few deep small clusters ($z > 11$ km). The seismic activity at shallow depth overlaps with a region of brittle rheological behavior (Figure 4d) and high σ_C (Figure 8c), between two areas with ductile rheology and lower σ_C, further suggesting that the base of the AU does not constitute a level of ductile décollement in several sectors of the VA.

The seismic cluster associated with the PL is characterized by several events showing prevalent normal-fault kinematics, but a high degree of variability in the strike, dip, and rake of the focal planes (Stabile, Giocoli, Lapenna, et al., 2014). This suggests that deformation is not accommodated by a single fault plane, but rather by a series of minor structures within the sedimentary cover. In our model (case C), this cluster of seismicity overlaps with a region of high $\dot{\varepsilon}_{II}$ (Figure 3j) and brittle behavior (Figure 4d) in both the AU and the ACP, where it is predicted the presence of several structures antithetic to the Mts. Maddalena Fault System and the Eastern Agri Fault System, which intersect each other. These faults show pronounced variations in the dip angle and also opposite dips, coherently with the lack of a preferential fault plane generating this cluster highlighted in previous studies (e.g., Stabile, Giocoli, Lapenna, et al., 2014; Valoroso et al., 2009). The brittle-ductile transition within the ACP is located at a depth of ≃6 km in our model, matching the maximum depth of this seismicity cluster and suggesting that seismic activity is subjected to a rheological control.

The seismicity associated with the wastewater reinjection in the CM2 well highlights the presence of the minor CMF. As highlighted by Hager et al. (2021), we observed in case C the formation of a high $\dot{\varepsilon}_{II}$ structure within the ACP with NE-ward dip (Figure 3j), that matches the position of the Costa Molina cluster, allowing us to identify this structure with the CMF. Also in this case, the base of the AU constitutes a rheological limit that hampers the upward propagation of the CMF, and subsequently of the seismicity.

We have carried out estimations of the σ_C for both the Pertusillo and the Costa Molina areas (Figure 8). Results show that, even without fluids, $\sigma_C > 0$ for most sedimentary cover, with the highest values in the areas NE of the VA and at a depth shallower than 6 km. This result suggests that both the CMF and the fracture network that generates the PL seismic cluster were prone to generate seismic activity. However, fluid presence along these structures produces a noticeable increase in σ_C, making them the regions of our model where σ_C is the highest within the sedimentary cover.

4.4. Parameter Sensitivity

The simulations carried out to test the sensitivity of our model to variations of selected parameters (see Section 3.5) have been compared with our reference cases B and C. Results are shown in Figures S2 and S3 of the Supporting Information S1, and summarized as follows:

1. Variations of d_F (cases A, D) do not cause major changes in the final geometry of our simulated VA, with the formation of two main border fault systems surrounding a basin subjected to subsidence. However, remarkable differences can still be observed when we consider the final width of the basin and the $\dot{\varepsilon}_{II}$ distribution at the end of our simulations. When $d_f = 2.5$ km (case A), the VA has a width of ≃10 km and is characterized by a relatively high $\dot{\varepsilon}_{II}$ between the border faults, whereas NE of VA we do not observe the formation of any structure that could generate the CM2 seismicity cluster. On the other hand, when $d_f = 10$ km (case D), there are several structures that could generate seismicity NE of the VA, but the final extension of the basin is ≃20 km, with deformation mostly occurring in the NE part of the valley. Therefore, values of $d_F = 5$ km or 7.5 km are more representative of the VA formation.
2. When $q_{0,s} = 45$ or 40 mW m^{-2} (cases E, F, G, H), the geometric relationships between the active structures in these simulations are similar to what we observe in our reference cases B and C, except for a flatter topographic profile and an extension ≃15 km for the basin in case H. However, qz values show remarkable variations, with values slightly above 45 mW m^{-2} on the topographic reliefs and ≃40 mW m^{-2} within the basin, when $q_{0,s} = 45$ mW m^{-2} (cases E, G). Variations are even more pronounced when $q_{0,s} = 40$ mW m^{-2}, with $q_z < 45$ mW m^{-2} on topographic reliefs and $q_z \simeq 35$ mW m^{-2} within the basin. These values do not correspond to what is reported in previous studies, in contrast with the q_z estimations obtained when the geotherm is calculated by imposing $q_{0,s} = 50$ mW m^{-2}.
3. The compressional velocity v_x^C (cases I, J, K, L) does not have a major impact on the tectonic setting of the VA when $d_{FZ} = 5$ km. However, in cases I and J, we observe a slight decrease in the width of the VA basin, with a distance of <10 km between the border faults at the end of the simulation. More importantly, however, the topography of the region shows remarkable differences with respect to our reference models. When $v_x^C = 3$ mm yr^{-1} (case I), the model predicts $h < 600$ m NE of the VA, and $h < -300$ m within the basin. Differently for $v_x^C = 7$ mm yr^{-1} (case J), $h \simeq 2{,}000$ m on the reliefs surrounding the VA, and $h > 700$ m within the VA. Similar results are obtained when $d_{FZ} = 7.5$ km (cases K, L), but the width of the VA in these simulations is ≃20 km, with the generation of several faults within and outside the main basin that have not been observed in the VA region.
4. If the erosion effect is removed ($\zeta = 0$, cases M, N), or strongly reduced ($\zeta = 10^{-8}$ m^2 s^{-1}, case O), we do not observe pronounced differences in the final tectonic setting of the VA and the surrounding region, except for a slightly increased activity of the faults NE and SW of the basin. However, the topography shows a profile that cannot be compared with the VA region, with $h > 2{,}200$ m SW of the basin and $h < -400$ m within the VA.
5. We have observed that η_{EFF} of the BF is the parameter that has the greater impact on the evolution and final geometry of the VA (cases P, Q, R, S, T, U). When the BF has high values of η_{EFF} (cases P, S) everywhere in the model, we do not observe the formation of a sedimentary basin surrounded by border faults, but rather by several structures cross-cutting all the layers throughout the entire model domain. This behavior is also observed in cases Q, R, T, and U, in the regions with high η_{EFF} values. In these simulations, the topographic difference between the basin and the surrounding reliefs is less than what is observed at the present day in the Southern Apennines region, with a negligible elevation of the reliefs in the proximity of the basin from the side with high η_{EFF}.
6. Another parameter that has a great impact on our results is the presence and number of preexisting faults in the ACP at the simulation onset (cases V, W). If only one fault is implemented (case V), the width of the VA at the end of the simulation is ≃8 km, with a maximum elevation of the region <1,300 m and almost no deformation between the border faults. However, the comparison between the tectonic structure obtained in this case and the seismic database does not show good matches between the location of the hypocenters and the fault geometry at the end of the simulation. If no faults are implemented in the ACP (case W), we do not observe the formation of a basin, but of a region of diffuse deformation within the sedimentary cover, where the topography is almost flat and structures with antithetic dip cross-cut the AU and the ACP.
7. When the extension is confined within the sedimentary cover (cases X, Y), the structures that we observe are not dissimilar from the ones observed, respectively, in cases B and C. Some differences in the sedimentary cover can be observed NE of the VA, where the structures in our reference models are substituted by a region

of more diffuse deformation. The main differences, however, occur in the crystalline basement, where we do not observe structures that can generate the small clusters of seismicity observed at a depth >11 km (Figures 3 and 4). Therefore, we can hypothesize that extension is not only confined to the sedimentary cover of the VA region but extends to the entire crust.

8. Last tests have been performed with $W_{FZ} = 1$ km (case Z) and $W_{FZ} = 4$ (case AA). In addition, we have considered a case study where there is only one weak region with $W_{FZ} = 8$ km (case AB). Our model shows that case Z is very similar to case W, with an overall flat topography and only a slight increase in strain in the region NE of the preexisting faults. On the other hand, in case AA we have a marked deformation that is not concentrated in proximity of the VA border faults, but rather in the central region of the basin. This differs from the present-day observations in the VA, where most seismicity is concentrated along the border faults. In case AB, the presence of a large fractures area at the center of the model causes the occurrence of two main fault systems, with a basin >10 km large and without any external structure, that could generate seismicity.

The choice of the simulations shown in this study stems from a bulk of more than 100 tests made on the model's reference configurations. For the sake of conciseness, several other simulations are not shown. To provide a few examples, variations of 1–2 km in the thickness of the layers composing our model do not cause noticeable variations in the final structural setting or rheological behavior of the study area. Similarly, variations of the mineral associations composing the polyphase AU and CB layers, within the range of ±5% of "high viscosity minerals" (e.g., garnet and pyroxene) with respect to "low viscosity" minerals (e.g., phyllosilicates and quartz) do not lead to noticeable variations in our results.

5. Discussion

The deformation that led to the overall geometry of the Southern Apennines is a matter of intense and partly unsolved debate, despite the extensive geological and geophysical surveys (e.g., Butler et al., 2005; Improta & Corciulo, 2006; Mazzoli et al., 2001; Mazzotti et al., 2000; Menardi Noguera & Rea, 2000; Patacca & Scandone, 2001; Scrocca et al., 2003, 2005; Speranza & Chiappini, 2002; Steckler et al., 2008). At the present day, one interpretation of the deformation recorded by the Southern Apennines suggests that this took place by a mechanism of thin-skinned tectonics. According to the thin-skinned tectonics model, deformation is confined in tectonic nappes within the SC, and does not involve the underlying CB (e.g., Mazzotti et al., 2000; Patacca & Scandone, 2001; Scrocca et al., 2005). For this mechanism to take place, most authors have invoked the presence of two major décollement levels. The lower décollement is located either within the BF (e.g., Marsella et al., 1995), or locally within the ACP (e.g., Mazzotti et al., 2000), while the upper décollement interval has been identified within the mélange zone at the base of the AU (Casero et al., 1988, 1991). In this scenario, the ACP represented a strain transfer zone located between two detachment levels, with the formation of a duplex structure affecting the Apulian carbonates. Subsequently, this structure has been deformed by the development of an indentor thrust within the Apulian crust (Casero et al., 1991). Alternatively, other interpretations suggest mechanisms of thick-skinned tectonics for the formation of the SA (e.g., Improta & Corciulo, 2006; Roure et al., 1991; Speranza & Chiappini, 2002; Steckler et al., 2008) where deeper structures involve the CB which is thereby incorporated in the thrust and fold belt. The origin and the presence of these structures in the CB are one of the main uncertainties of the deep SA. In this respect, Scrocca et al. (2005) hypothesize that faulting may propagate from a main detachment level within the subducting lithosphere, whereas Shiner, Mazzoli, and Cello (2004) invoke the inversion of inherited synsedimentary normal faults, controlling the deposition of Permo-Triassic basins below the ACP. Deformation in the Southern Apennines has also been interpreted as a combination of thin-skinned tectonics and thick-skinned tectonics (Menardi Noguera & Rea, 2000), with the former characterizing the shallower crustal levels of the Apennines, and the latter mostly concentrated in the deeper parts, with structures reaching the Adriatic Moho. Similar conclusions have been reached in the study by Turrini and Rennison (2004), which indicates thick-skinned tectonics in the internal domains of the Apennines and thin-skinned tectonics in the external domains. Roure et al. (2012) indicate that thin-skinned tectonics was active up to the Pliocene-Quaternary in the Southern Apennines and along the eastern margins of the Ionian abyssal plain, whereas it is not more recent than the upper Miocene in other regions of the African margin (i.e., Algeria).

In the VA, Shiner, Beccacini, and Mazzoli (2004) suggest that deformation occurs by thick-skinned tectonics within the ACP, although the authors do not exclude the presence of other areas where thin-skinned tectonics is predominant, while Valoroso et al. (2011), identify a thin-skinned-to-thick-skinned tectonics switch during the late Pliocene. In our model, we have observed that the presence of preexisting faults in the ACP, reactivated both

during the late Pliocene-early Pleistocene contractional phase and the subsequent extensional phase, is one of the factors that cause the formation of the Eastern Agri Fault System and the Mts. Maddalena Fault System. Both these border faults and the structures within the VA crosscut the ACP and the overlying AU. Due to the low values of η_{EFF} in the BF, the faults located within the ACP do not propagate into the CB, but they rather flatten up in correspondence of the BF layer. However, a few high-angle structures with high $\dot{\varepsilon}_{II}$ are also detected in the CB region with brittle behavior. The presence of these active faults is confirmed by seismic activity at a depth >11 km (Frepoli et al., 2005; Panebianco et al., 2023), whereas a smaller number of events is observed in the region between 6 and 11 km (Figure 3), especially in the southern sector of the VA. The evolution of the VA domain in our model shows that this deformation pattern is preserved over the whole duration of the Quaternary compressive-extensional history, and does not mutate even for regions of the model where the BF is thinned to ≃1 km (Figure 3). We therefore suggest that the VA and surrounding domains are mostly subjected to thin-skinned tectonics, in a scenario where deformation in the SC and the CB is decoupled along the BF. Further evidence of the décollement between SC and CB is the marked deformation of the top BF (Figure 3), forming pronounced anticlines in the central region of the model during the final phases of the simulation. Similar km-scale anticlines defined by the geometry of the top ACP have been observed in previous studies not only in the VA (Nicolai & Gambini, 2007; Valoroso et al., 2011), but also in the Northern Apennines (Bonini & Sani, 2002), where the BF has also been interpreted as a décollement layer between the SC formations and the CB.

During the simulation of the contractional phase, we observe an overall uplifting of the entire area circumscribed by the preexisting faults in the ACP. The following extensional phase is characterized by subsidence of most of the previously uplifting region, with a migration of the active fault segments rightwards in the NE VA (Figure 4a) and leftwards in the SW VA (Figure 4c). This velocity pattern may imply the presence of a NE-trending transfer structure separating the two sectors of the VA, with unknown seismic features. The importance of NE-trending faults in separating different structurally coherent sectors of the VA is outlined by Palladino et al. (2023).

A remarkable characteristic of the VA velocity field is its step-wise pattern, which can be observed both at depth within the SC (Figure 4) and at the surface (Figures 5 and 6) and leads to a primarily fault-controlled deformation in this region. This hypothesis is supported by geomorphologic and hydrographic evidence of the area (Giano, 2016; Maschio et al., 2005), and further highlights the role exerted by the reactivation of preexisting structures for the Neogene extensional deformation in the VA. More in detail, we observe higher v_z values in the proximity of the Eastern Agri Fault System in the NE VA and in the proximity of the Mts. Maddalena Fault System in the SW VA, potentially reflecting the higher seismogenic potential of these border fault segments in these sections of the basin, coherently with findings of Maschio et al. (2005, and references therein).

Both the CMF and the Caldarosa Fault in case C do not appear in our model as single, isolated structures, but rather as part of a diffuse zone of brittle deformation NE of the VA, that lasts for most of the extensional history of the region. The activity of these faults during the last stages of simulation strongly decreased but is not completely extinguished. Coherently, seismicity along the CMF was almost completely absent before the onset of wastewater disposal in the CM2 (Hager et al., 2021; Stabile, Giocoli, Perrone, et al., 2014). However, the calculated values of the $\dot{\varepsilon}_{II}$ along the CMF suggest that this fault was not completely aseismic before fluid reinjection. This assumption is supported by our estimations of the σ_C along the fault, clearly showing that even in dry conditions (Figures 8a and 8e) the CMF was a fault with considerable seismic potential. After the fluid reinjection, it is possible to observe a peak in the CMF σ_C values (Figures 8b, 8c, and 8e), making this fault the interval with the highest seismic potential in the sedimentary cover located NE-ward of the VA. Despite fluid-injection operations at the CM2 well, induced seismic events with a magnitude (Ml) greater than 2.0 were never observed. This is attributed to the hydraulic connection between the injection site and the production area within the VA oil field (Stabile & Telesca, 2023). In other terms, the peak in CMF σ_C values is solely a result of the local buildup in pore pressure, as a gradual increase of vertical stress due to mass accumulation is not feasible at the CM2 site. Similar conditions are also observed in the region of the ACP that is affected by water loading from the PL (Figure 8) (e.g., Stabile, Giocoli, Lapenna, et al., 2014; Stabile et al., 2015). The earthquake cluster in this area is associated with the activation of small and shallow fault segments with a variable dip near the southern termination of the Mts. Maddalena Fault System (Valoroso et al., 2009). In this region of concentrated seismic activity, values of σ_C were already above 0 before the presence of the artificial reservoir, but the presence of water at hydrostatic pressure

caused a pronounced increase of the σ_C values, especially between 2 and 5 km. An important issue raised by our work is the presence of several regions within and outside the VA characterized by $\sigma_C > 0$. Consequently, the reinjection of fluids in this area should be considered a high-risk activity, given the presence of a thick brittle layer in the ACP, and the potentially high number of faults in the SC of the VA and surrounding areas.

6. Conclusions

The Val d'Agri represents an interesting case study where the interactions between fluids and host rocks lead to induced seismicity in a region already characterized by high seismic hazard. However, a correct estimation of the hazard cannot be assessed without a knowledge of the mechanisms behind the present-day tectonics and therefore, a quantitative analysis of the stress fields that characterize the area. We show that the strength and rheology stratification of the crust in the Val d'Agri leads to predominant mechanisms of thin-skinned tectonics that drive the formation and evolution of the region, with the Burano Formation acting as a décollement layer and a rheological boundary between the deformation of the sedimentary cover and the crystalline basement. Differently, the base of the allochthonous units, although with ductile behavior, do not constitute a rheological barrier for the propagation at depth of the Monti della Maddalena Fault System and the Eastern Agri Fault System. On the contrary, the high $\dot{\varepsilon}_{II}$ values that characterize the intervals where the preexisting faults are located drive the rheology of the basal intervals of the allochthonous units, that in such conditions have a brittle behavior. However, our model does not exclude the presence of regions within the Burano Formation where a high carbonate %vol. may favor the propagation of sedimentary cover structures in the crystalline basement, especially in the NW Val d'Agri, where the correspondence between our model and the hypocenter location is slightly worse than in the SE Val d'Agri.

Our model predicts the presence of two main regions where seismic activity is favored by the presence of brittle lithologies. The shallower region occurs within the Apulian Carbonatic Platform, at a depth shallower than 6 km, and its base corresponds with the brittle-ductile transition of the carbonate rocks. The other is located at a depth between ≃11 and ≃15 km. Its top boundary consists of the Burano Formation-crystalline basement boundary, while the lower boundary is constituted by the brittle-ductile transition of the crystalline basement. A key aspect of our study is represented by the quantification of the Coulomb stress (σ_C) values, especially in the layers with brittle behavior. Our model clearly shows that $\sigma_C > 0$ in several areas of the investigated domain, with the highest values in the Apulian Carbonatic Platform. As a consequence, particular attention should be paid to all those activities that include the injection of fluids underground, especially taking into account the presence of favorably oriented, unknown faults that could be easily reactivated by an increase in fluid pressure.

Acronyms

ACP	Apulian Carbonate Platform
AU	Allochthonous units
BF	Burano Formation
CB	Crystalline Basement
CM2	Costa Molina 2
CMF	Costa Molina Fault
PL	Pertusillo lake
SC	Sedimentary Cover
VA	Val d'Agri

Data Availability Statement

ASPECT 2.3.0 is an open-source code, accessible from https://aspect.geodynamics.org/.

All input files to reproduce the results of this paper and the Earthquake Location Data set are available from https://data.mendeley.com/datasets/yt32237dp3/1 (Lavecchia et al., 2024).

Acknowledgments
This study was carried out within the RETURN Extended Partnership and received funding from the European Union—NextGenerationEU (National Recovery and Resilience Plan—NRRP, Mission 4, Component 2, Investment 1.3—D.D. 1243 2/8/2022, PE0000005). This research partially benefited from the support of the PRIN-MUR 2022 project "Multiscale study of seismogenic processes in Campania-Lucania Apennines using machine learning algorithms and multiparametric observations (FRACTURES)", Grant 2022BEKFN2, funded by the European Union—NextGenerationEU. Vincenzo Serlenga is currently funded by the project ITINERIS "Italian Integrated Environmental Research Infrastructures System" (National Recovery and Resilience Plan—NRRP, Mission 4, Component 2, Investment 3.1—Project code IR0000032, funded by the European Union—NextGenerationEU). Open access publishing facilitated by Universita degli Studi di Bari Aldo Moro, as part of the Wiley - CRUI-CARE agreement.

References

Albaric, J., Oye, V., Langet, N., Hasting, M., Lecomte, I., Iranpour, K., et al. (2014). Monitoring of induced seismicity during the first geothermal reservoir stimulation at Paralana, Australia. *Geothermics*, *52*, 120–131. https://doi.org/10.1016/j.geothermics.2013.10.013

Aliaj, S. (2006). The Albanian orogen: Convergence zone between Eurasia and the Adria microplate. In N. Pinter, G. Gyula, J. Weber, S. Stein, & D. Medak (Eds.), *The Adria microplate: GPS geodesy, tectonics and hazards* (pp. 133–149).

Alt, I., Richard, C., & Zoback, M. D. (2016). In situ stress and active faulting in Oklahoma. *Bulletin of the Seismological Society of America*, *107*(1), 216–228. https://doi.org/10.1785/0120160156

Amato, A., & Montone, P. (1997). Present-day stress field and active tectonics in southern peninsular Italy. *Geophysical Journal International*, *130*(2), 519–534. https://doi.org/10.1111/j.1365-246X.1997.tb05666.x

Ascione, A., Ciarcia, S., Di Donato, V., Mazzoli, S., & Vitale, S. (2012). The Pliocene-Quaternary wedge-top basins of southern Italy: An expression of propagating lateral slab tear beneath the Apennines. *Basin Research*, *24*(4), 456–474. https://doi.org/10.1111/j.1365-2117.2011.00534.x

Audin, L., Avouac, J., Flouzat, M., & Plantet, J. (2002). Fluid-driven seismicity in a stable tectonic context: The Remiremont fault zone, Vosges, France. *Geophysical Research Letters*, *29*(6), 13-1–13-4. https://doi.org/10.1029/2001GL012988

Bailey, R. (2006). Large time step numerical modelling of the flow of Maxwell materials. *Geophysical Journal International*, *164*(2), 460–466. https://doi.org/10.1111/j.1365-246X.2005.02788.x

Baisch, S., Vörös, R., Rothert, E., Stang, H., Jung, R., & Schellschmidt, R. (2010). A numerical model for fluid injection induced seismicity at Soultz-sous-Forêts. *International Journal of Rock Mechanics and Mining Sciences*, *47*(3), 405–413. https://doi.org/10.1016/j.ijrmms.2009.10.001

Balasco, M., Cavalcante, F., Romano, G., Serlenga, V., Siniscalchi, A., Stabile, T. A., & Lapenna, V. (2021). New insights into the High Agri Valley deep structure revealed by magnetotelluric imaging and seismic tomography (southern Apennine, Italy). *Tectonophysics*, *808*(22881), 7. https://doi.org/10.1016/j.tecto.2021.228817

Ballato, P., Brune, S., & Strecker, M. R. (2019). Sedimentary loading–unloading cycles and faulting in intermontane basins: Insights from numerical modeling and field observations in the NW Argentine Andes. *Earth and Planetary Science Letters*, *506*, 388–396. https://doi.org/10.1016/j.epsl.2018.10.043

Benedetti, L., Tapponnier, P., King, G., & Piccardi, L. (2002). Surface rupture of the 1857 southern Italian earthquake? *Terra Nova*, *10*(4), 206–210. https://doi.org/10.1046/j.1365-3121.1998.00189.x

Benson, P., Austria, D., Gehne, S., Butcher, E., Harnett, C., Fazio, M., et al. (2020). Laboratory simulations of fluid-induced seismicity, hydraulic fracture, and fluid flow. *Geomechanics for Energy and the Environment*, *24*, 100169. https://doi.org/10.1016/j.gete.2019.100169

Billen, M., & Hirth, G. (2007). Rheologic controls on slab dynamics. *Geochemistry, Geophysics, Geosystems*, *8*(8), Q08012. https://doi.org/10.1029/2007GC001597

Bonardi, G., Di Nocera, S., Sgrosso, I., Brancaccio, L., Cinque, A., Morra, V., et al. (1988). Carta geologica dell'Appennino meridionale 1:250.000. In G. Bonardi, B. D'Argenio, & V. Perrone (Eds.), *74° congresso della società geologica italiana, 13-17 settembre 1988*. Dipartimento di Scienze della Terra Università di Napoli, Consiglio Nazionale delle Ricerche.

Bonini, M., & Sani, F. (2002). Extension and compression in the Northern Apennines (Italy) hinterland: Evidence from the late Miocene-Pliocene Siena-Radicofani Basin and relations with basement structures. *Tectonics*, *21*(3). https://doi.org/10.1029/2001tc900024

Boschi, E., Guidoboni, E., Ferrari, G., Mariotti, D., Valensise, G., & Gasperini, P. (2000). Catalogue of strong Italian earthquakes from 461 BC to 1997 (appendix to volume 43 N ° 4, 2000). *Annals of Geophysics*, *43*(4).

Brune, S., Corti, G., & Ranalli, G. (2017). Controls of inherited lithospheric heterogeneity on rift linkage: Numerical and analog models of interaction between the Kenyan and Ethiopian rifts across the Turkana depression. *Tectonics*, *36*(9), 1767–1786. https://doi.org/10.1002/2017TC004739

Buiter, S., Wortel, M., & Govers, R. (1998). The role of subduction in the evolution of the Apennines foreland basin. *Tectonophysics*, *296*(3), 249–268. https://doi.org/10.1016/S0040-1951(98)00158-9

Burov, E., & Poliakov, A. (2001). Erosion and rheology controls on synrift and postrift evolution: Verifying old and new ideas using a fully coupled numerical model. *Journal of Geophysical Research*, *106*(B8), 16461–16481. https://doi.org/10.1029/2001JB000433

Butler, R., Mazzoli, S., Corrado, S., De Donatis, M., Di Bucci, D., Gambini, R., et al. (2005). Applying thick-skinned tectonic models to the Apennine thrust belt of Italy—Limitations and implications. *AAPG Memoir*, *82*, 647–667.

Buttinelli, M., Improta, L., Bagh, S., & Chiarabba, C. (2016). Inversion of inherited thrusts by wastewater injection induced seismicity at the Val d'Agri oilfield (Italy). *Scientific Reports*, *6*(1), 37165. https://doi.org/10.1038/srep37165

Carbone, S., Catalano, S., Lazzari, S., Lentini, F., & Monaco, C. (1991). Presentazione della carta geologica del bacino del fiume Agri (Basilicata). *Memorie della Societa Geologica Italiana*, *47*, 129–143.

Casero, P., Roure, F., Endignoux, L., Moretti, I., Muller, C., Sage, L., & Vially, R. (1988). Neogene geodynamic evolution of the southern Apennines. *Memorie della Societa Geologica Italiana*, *41*, 109–120.

Casero, P., Roure, F., & Vially, R. (1991). Tectonic framework and petroleum potential of the southern Apennines accretionary wedge. *European Association of Petroleum Geoscientists, Special Publication*, *1*, 381–387.

Cataldi, R., Mongelli, F., Squarci, P., Taffi, L., Zito, G., & Calore, C. (1995). Geothermal ranking of Italian territory. *Geothermics*, *24*(1), 115–129. https://doi.org/10.1016/0375-6505(94)00026-9

Cello, G., & Mazzoli, S. (1998). Apennine tectonics in southern Italy: A review. *Journal of Geodynamics*, *27*(2), 191–211. https://doi.org/10.1016/S0264-3707(97)00072-0

Cello, G., Tondi, E., Micarelli, L., & Mattioni, L. (2003). Active tectonics and earthquake sources in the epicentral area of the 1857 Basilicata earthquake (southern Italy). *Journal of Geodynamics*, *36*(1–2), 37–50. https://doi.org/10.1016/S0264-3707(03)00037-1

Cinque, A., Patacca, E., Scandone, P., & Tozzi, M. (1993). Quaternary kinematic evolution of the southern Appennines. Relationships between surface geological features and deep lithospheric structures. *Annals of Geophysics*, *36*(2). https://doi.org/10.4401/ag-4283

Colella, A., Lapenna, V., & Rizzo, E. (2004). High-resolution imaging of the High Agri Valley basin (southern Italy) with electrical resistivity tomography. *Tectonophysics*, *386*(1–2), 29–40. https://doi.org/10.1016/j.tecto.2004.03.017

Corti, G., Ranalli, G., Mulugeta, G., Agostini, A., Sani, F., & Zugu, A. (2010). Control of the rheological structure of the lithosphere on the inward migration of tectonic activity during continental rifting. *Tectonophysics*, *490*(3–4), 165–172. https://doi.org/10.1016/j.tecto.2010.05.004

Curbelo, J., Duarte, L., Albousière, T., Dubuffet, F., Labrosse, S., & Ricard, Y. (2019). Numerical solutions of compressible convection with an infinite Prandtl number: Comparison of the anelastic and anelastic liquid models with the exact equations. *Journal of Fluid Mechanics*, *873*, 646–687. https://doi.org/10.1017/jfm.2019.420

D'Agostino, N. (2014). Complete seismic release of tectonic strain and earthquake recurrence in the Apennines (Italy). *Geophysical Research Letters*, *41*(4), 1155–1162. https://doi.org/10.1002/2014GL059230

D'Agostino, N., Avallone, A., Cheloni, D., D'Anastasio, E., Mantenuto, S., & Selvaggi, G. (2008). Active tectonics of the Adriatic region from GPS and earthquake slip vectors. *Journal of Geophysical Research*, *113*(12), B12413. https://doi.org/10.1029/2008jb005860

Del Ben, A., Geletti, R., & Mocnik, A. (2010). Relation between recent tectonics and Mesozoic inherited structures of the central-southern Adria plate. *Bollettino di Geofisica Teorica e Applicata*, *51*(2–3), 99–115.

Dell'Aversana, P. (2003). Integration loop of global offset seismic, continuous profiling magnetotelluric and gravity data. *First Break*, *21*(11), 32–41. https://doi.org/10.3997/1365-2397.2003019

Deng, Q., Blöcher, G., Cacace, M., & Schmittbuhl, J. (2021). Modeling of fluid-induced seismicity during injection and after shut-in. *Computers and Geotechnics*, *140*, 104489. https://doi.org/10.1016/j.compgeo.2021.104489

Doglioni, C. (1991). A proposal for the kinematic modelling of w-dipping subductions—Possible applications to the Tyrrhenian-Apennines system. *Terra Nova*, *3*(4), 423–434. https://doi.org/10.1111/j.1365-3121.1991.tb00172.x

Doglioni, C., Harabaglia, P., Martinelli, G., Mongelli, F., & Zito, G. (1996). A geodynamic model of the southern Apennines accretionary prism. *Terra Nova*, *8*(6), 540–547. https://doi.org/10.1111/j.1365-3121.1996.tb00783.x

Doglioni, C., Harabaglia, P., Merlini, S., Mongelli, F., Peccerillo, A., & Piromallo, C. (1999). Orogens and slabs vs. their direction of subduction. *Earth-Science Reviews*, *45*(3), 167–208. https://doi.org/10.1016/S0012-8252(98)00045-2

Ebinger, C. (2005). Continental breakup: The East African perspective. *Astronomy and Geophysics*, *46*(2), 2–16. https://doi.org/10.1111/j.1468-4004.2005.46216.x

El Hariri, M., Abercrombie, R., Rowe, C., & do Nascimento, A. (2010). The role of fluids in triggering earthquakes: Observations from reservoir induced seismicity in Brazil. *Geophysical Journal International*, *181*(3), 1566–1574. https://doi.org/10.1111/j.1365-246X.2010.04554.x

Evans, K. F., Moriya, H., Niitsuma, H., Jones, R. H., Phillips, W. S., Genter, A., et al. (2005). Microseismicity and permeability enhancement of hydrogeologic structures during massive fluid injections into granite at 3 km depth at the Soultz HDR site. *Geophysical Journal International*, *160*(1), 388–412. https://doi.org/10.1111/j.1365-246X.2004.02474.x

Filippucci, M., Tallarico, A., Dragoni, M., & de Lorenzo, S. (2019). Relationship between depth of seismicity and heat flow: The case of the Gargano area (Italy). *Pure and Applied Geophysics*, *176*(6), 2383–2394. https://doi.org/10.1007/s00024-019-02107-5

Frepoli, A., Cinti, F., Amicucci, L., Cimini, G., De Gori, P., & Pierdominici, S. (2005). Pattern of seismicity in the Lucanian Apennines and foredeep (southern Italy) from recording by SAPTEX temporary array. *Annals of Geophysics*, *48*, 1035–1054. https://doi.org/10.4401/ag-3252

Gardonio, B., Jolivet, R., Calais, E., & Leclère, H. (2018). The April 2017 Mw6.5 Botswana earthquake: An intraplate event triggered by deep fluids. *Geophysical Research Letters*, *45*(17), 8886–8896. https://doi.org/10.1029/2018GL078297

Gerya, T. (2019). Numerical solution of the heat conservation equation. In *Introduction to numerical geodynamic modelling* (2nd ed., pp. 139–155). Cambridge University Press. https://doi.org/10.1017/9781316534243.011

Gerya, T., Perchuk, L., van Reenen, D., & Andre Smit, C. (2000). Two-dimensional numerical modeling of pressure–temperature-time paths for the exhumation of some granulite facies terrains in the Precambrian. *Journal of Geodynamics*, *30*(1), 17–35. https://doi.org/10.1016/S0264-3707(99)00025-3

Giano, S. I. (2016). Geomorphology of the Agri intermontane basin (Val d'Agri-Lagonegrese National Park, southern Italy). *Journal of Maps*, *12*(4), 639–648. https://doi.org/10.1080/17445647.2015.1068715

Gogus, O., & Ueda, K. (2018). Peeling back the lithosphere: Controlling parameters, surface expressions and the future directions in delamination modeling. *Journal of Geodynamics*, *117*, 21–40. https://doi.org/10.1016/j.jog.2018.03.003

Gueguen, E., Doglioni, C., & Fernandez, M. (1998). On the post-25 Ma geodynamic evolution of the western Mediterranean. *Tectonophysics*, *298*(1), 259–269. https://doi.org/10.1016/S0040-1951(98)00189-9

Hager, B., Dieterich, J., Frohlich, C., Juanes, R., Mantica, S., Shaw, J., et al. (2021). A process-based approach to understanding and managing triggered seismicity. *Nature*, *595*(7869), 684–689. https://doi.org/10.1038/s41586-021-03668-z

Harris, R. A. (1998). Introduction to special section: Stress triggers, stress shadows, and implications for seismic hazard. *Journal of Geophysical Research*, *103*(B10), 24347–24358. https://doi.org/10.1029/98JB01576

Hasterok, D., Gard, M., & Webb, J. (2018). On the radiogenic heat production of metamorphic, igneous, and sedimentary rocks. *Geoscience Frontiers*, *9*(6), 1777–1794. https://doi.org/10.1016/j.gsf.2017.10.012

Healy, J. H., Rubey, W. W., Griggs, D. T., & Raleigh, C. B. (1968). The Denver earthquakes. *Science*, *161*(3848), 1301–1310. https://doi.org/10.1126/science.161.3848.1301

Hearn, E. H., Koltermann, C., & Rubinstein, J. L. (2018). Numerical models of pore pressure and stress changes along basement faults due to wastewater injection: Applications to the 2014 Milan, Kansas earthquake. *Geochemistry, Geophysics, Geosystems*, *19*(4), 1178–1198. https://doi.org/10.1002/2017GC007194

Holton, J. (1999). Four geologic settings dominate oil, gas fields of Italy, Sicily. *Oil & Gas Journal*, *97*(49), 81–84.

Hsieh, P. A., & Bredehoeft, J. D. (1981). A reservoir analysis of the Denver earthquakes: A case of induced seismicity. *Journal of Geophysical Research*, *86*(B2), 903–920. https://doi.org/10.1029/JB086iB02p00903

Huismans, R., & Beaumont, C. (2011). Depth-dependent extension, two-stage breakup and cratonic underplating at rifted margins. *Nature*, *473*(7345), 74–79. https://doi.org/10.1038/nature09988

Improta, L., Bagh, S., De Gori, P., Valoroso, L., Pastori, M., Piccinini, D., et al. (2017). Reservoir structure and wastewater-induced seismicity at the Val d'Agri oilfield (Italy) shown by three-dimensional V_p and V_p/V_s local earthquake tomography. *Journal of Geophysical Research: Solid Earth*, *122*(11), 9050–9082. https://doi.org/10.1002/2017JB014725

Improta, L., & Corciulo, M. (2006). Controlled source nonlinear tomography: A powerful tool to constrain tectonic models of the southern Apennines orogenic wedge, Italy. *Geology*, *34*(11), 941–944. https://doi.org/10.1130/G22676A.1

Improta, L., De Gori, P., & Chiarabba, C. (2014). New insights into crustal structure, Cenozoic magmatism, CO_2 degassing, and seismogenesis in the southern Apennines and Irpinia region from local earthquake tomography. *Journal of Geophysical Research: Solid Earth*, *119*(11), 8283–8311. (cited By 21). https://doi.org/10.1002/2013jb010890

Irgens, F. (2008). *Continuum mechanics*. (p. 661). Springer Science & Business Media.

Jaupart, C., Mareschal, J.-C., & Iarotsky, L. (2016). Radiogenic heat production in the continental crust. *Lithos*, *262*, 398–427. https://doi.org/10.1016/j.lithos.2016.07.017

Ji, S., Zhao, P., & Xia, B. (2003). Flow laws of multiphase materials and rocks from end-member flow laws. *Tectonophysics*, *370*(1–4), 129–145. https://doi.org/10.1016/s0040-1951(03)00182-3

Kilb, D., Gomberg, J., & Bodin, P. (2002). Aftershock triggering by complete Coulomb stress changes. *Journal of Geophysical Research*, *107*(B4), ESE2-1–ESE2-14. https://doi.org/10.1029/2001JB000202

King, G. C. P., Stein, R. S., & Lin, J. (1994). Static stress changes and the triggering of earthquakes. *Bulletin of the Seismological Society of America*, *84*(3), 935–953. https://doi.org/10.1785/BSSA0840030935

Kronbichler, M., Heister, T., & Bangerth, W. (2012). High accuracy mantle convection simulation through modern numerical methods [Software]. *Geophysical Journal International*, *191*(1), 12–29. https://doi.org/10.1111/j.1365-246X.2012.05609.x

Lavecchia, A., Beekman, F., Clark, S., & Cloetingh, S. (2016). Thermo-rheological aspects of crustal evolution during continental breakup and melt intrusion: The Main Ethiopian Rift, East Africa. *Tectonophysics*, *686*, 51–62. https://doi.org/10.1016/j.tecto.2016.07.018

Lavecchia, A., Clark, S., Beekman, F., Cloetingh, S., & Burov, E. (2016). Thermal perturbation, mineral assemblages, and rheology variations induced by dyke emplacement in the crust. *Tectonics*, *35*(5), 1137–1152. https://doi.org/10.1002/2016TC004125

Lavecchia, A., Filippucci, M., Tallarico, A., Selvaggi, G., Cecere, G., & Cloetingh, S. (2022). Role of crustal fluids and thermo-mechanical structure for lower crustal seismicity: The Gargano promontory (southern Italy). *Global and Planetary Change*, *217*, 103929. https://doi.org/10.1016/j.gloplacha.2022.103929

Lavecchia, A., Serlenga, V., Filippucci, M., Stabile, T., Prosser, G., & Tallarico, A. (2024). Fault (re)activation and fluid-induced seismicity: An example from the Val d'Agri intermontane basin (southern Italy) [Dataset]. *Mendeley Data, V1*. https://doi.org/10.17632/yt32237dp3.1

Malinverno, A., & Ryan, W. B. F. (1986). Extension in the Tyrrhenian Sea and shortening in the Apennines as result of arc migration driven by sinking of the lithosphere. *Tectonics*, *5*(2), 227–245. https://doi.org/10.1029/TC005i002p00227

Marsella, E., Bally, A. W., Cippitelli, G., D'Argenio, B., & Pappone, G. (1995). Tectonic history of the Lagonegro Domain and southern Apennine thrust belt evolution. *Tectonophysics*, *252*(1), 307–330. https://doi.org/10.1016/0040-1951(95)00097-6

Maschio, L., Ferranti, L., & Burrato, P. (2005). Active extension in Val d'Agri area, southern Appenines, Italy: Implications for the geometry of seismogenic belt. *Geophysical Journal International*, *162*(2), 591–609. https://doi.org/10.1111/j.1365-246X.2005.02597.x

Mattavelli, L., Novelli, L., & Anelli, L. (1991). Generation, accumulation and production of Europe's hydrocarbons. Special publication of the European association of petroleum geoscientists. In A. Spencer (Ed.), *Generation, accumulation and production of Europe's hydrocarbons* (Vol. 1, pp. 369–380). Oxford University Press.

Maurer, J., Dunham, E. M., & Segall, P. (2020). Role of fluid injection on earthquake size in dynamic rupture simulations on rough faults. *Geophysical Research Letters*, *47*(13), e2020GL088377. https://doi.org/10.1029/2020GL088377

Mazzoli, S., Ascione, A., Candela, S., Iannace, A., Megna, A., Santini, S., & others (2013). Subduction and continental collision events in the southern Apennines: Constraints from two crustal cross-sections. *Rendiconti Online della Società Geologica Italiana*, *25*, 78–84. https://doi.org/10.3301/rol.2013.07

Mazzoli, S., Barkham, S., Cello, G., Gambini, R., Mattioni, L., Shiner, P., & Tondi, E. (2001). Reconstruction of continental margin architecture deformed by the contraction of Lagonegro Basin, southern Apennines, Italy. *Journal of the Geological Society of London*, *158*(2), 309–319. https://doi.org/10.1144/jgs.158.2.309

Mazzotti, A. P., Stucchi, E., Fradelizio, G. L., Zanzi, L., & Scandone, P. (2000). Seismic exploration in complex terrains: A processing experience in the southern Apennines. *Geophysics*, *65*(5), 1402–1417. https://doi.org/10.1190/1.1444830

Megna, A., Candela, S., Mazzoli, S., & Santini, S. (2014). An analytical model for the geotherm in the Basilicata oil fields area (southern Italy). *Italian Journal of Geoscience*, *133*(2), 204–213. https://doi.org/10.4401/ag-3510

Menardi Noguera, A., & Rea, G. (2000). Deep structure of the Campanian-Lucanian arc (southern Apennine, Italy). *Tectonophysics*, *324*(4), 239–265. https://doi.org/10.1016/S0040-1951(00)00137-2

Morandi, S., & Ceragioli, E. (2002). Integrated interpretation of seismic and resistivity images across the "Val d'Agri" graben (Italy). *Annals of Geophysics*, *45*(2). https://doi.org/10.4401/ag-7059

Nakagomi, K., Terakawa, T., Matsumoto, S., & Horikawa, S. (2021). Stress and pore fluid pressure control of seismicity rate changes following the 2016 Kumamoto earthquake, Japan. *Earth Planets and Space*, *73*(1), 11. https://doi.org/10.1186/s40623-020-01329-5

Nicolai, C., & Gambini, R. (2007). Structural architecture of the Adria platform-and-basin system. *Bollettino Societa' Geologica Italiana*, *7*, 21–37.

Palano, M., Cannavò, F., Ferranti, L., Mattia, M., & Mazzella, M. (2011). Strain and stress fields in the southern Apennines (Italy) constrained by geodetic, seismological and borehole data. *Geophysical Journal International*, *187*(3), 1270–1282. https://doi.org/10.1111/j.1365-246X.2011.05234.x

Palladino, G., Prosser, G., Olita, F., Avagliano, D., Dello Iacovo, B., Giano, S., et al. (2023). Reconstruction of the structural setting of the north-eastern side of the High Agri Valley (southern Apennines, Italy) based on detailed field mapping. *Journal of Maps*, *19*(1), 2257729. https://doi.org/10.1080/17445647.2023.2257729

Panebianco, S., Serlenga, V., Satriano, C., Cavalcante, F., & Stabile, T. A. (2023). Semi-automated template matching and machine-learning based analysis of the august 2020 Castelsaraceno microearthquake sequence (southern Italy). *Geomatics, Natural Hazards and Risk*, *14*(1), 2207715. https://doi.org/10.1080/19475705.2023.2207715

Paola, C. (2000). Quantitative models of sedimentary basin filling. *Sedimentology*, *47*(s1), 121–178. https://doi.org/10.1046/j.1365-3091.2000.00006.x

Patacca, E., Sartori, R., & Scandone, P. (1990). Tyrrhenian basin and Apenninic arcs: Kinematic relations since late Tortonian times. *Bollettino-Societa Geologica Italiana*, *45*, 425–451.

Patacca, E., & Scandone, P. (2001). Late thrust propagation and sedimentary response in the thrust-belt—Foredeep system of the southern Apennines (Pliocene-Pleistocene). In G. B. Vai, & I. P. Martini (Eds.), *Anatomy of an orogen: The Apennines and adjacent Mediterranean basins* (pp. 401–440). Springer Netherlands. https://doi.org/10.1007/978-94-015-9829-3_23

Patacca, E., Scandone, P., Di Luzio, E., Cavinato, G. P., & Parotto, M. (2008). Structural architecture of the central Apennines: Interpretation of the CROP 11 seismic profile from the Adriatic coast to the orographic divide. *Tectonics*, *27*(3). https://doi.org/10.1029/2005TC001917

Pedersen, R., Sigmundsson, F., & Masterlark, T. (2009). Rheologic controls on inter-rifting deformation of the northern volcanic zone, Iceland. *Earth and Planetary Science Letters*, *281*(1–2), 14–26. https://doi.org/10.1016/j.epsl.2009.02.003

Raleigh, C., Healy, J., & Bredehoeft, J. (1972). Faulting and crustal stress at Rangely, Colorado. *Geophysical Monograph Series*, *16*, 275–284. https://doi.org/10.1029/GM016p0275

Raleigh, C., Healy, J., & Bredehoeft, J. (1976). An experiment in earthquake control at Rangely, Colorado. *Science*, *191*(4233), 1230–1237. https://doi.org/10.1126/science.191.4233.1230

Ranalli, G. (1995). *Rheology of the Earth*. Chapman and Hall.

Ranalli, G. (2000). Rheology of the crust and its role in tectonics reactivation. *Journal of Geodynamics*, *30*(1–2), 3–15. https://doi.org/10.1016/S0264-3707(99)00024-1

Reasenberg, P. A., & Simpson, R. W. (1992). Response of regional seismicity to the static stress change produced by the Loma Prieta earthquake. *Science*, *255*(5052), 1687–1690. https://doi.org/10.1126/science.255.5052.1687

Rinaldi, A. P., Improta, L., Hainzl, S., Cataldi, F., Urpi, L., & Wiemer, S. (2020). Combined approach of poroelastic and earthquake nucleation applied to the reservoir-induced seismic activity in the Val d'Agri area, Italy. *Journal of Rock Mechanics and Geotechnical Engineering*, *12*(4), 802–810. https://doi.org/10.1016/j.jrmge.2020.04.003

Roure, F., Casero, P., & Addoum, B. (2012). Alpine inversion of the North African margin and delamination of its continental lithosphere. *Tectonics*, *31*(3), TC3006. https://doi.org/10.1029/2011TC002989

Roure, F., Casero, P., & Vially, R. (1991). Growth processes and melange formation in the southern Apennines accretionary wedge. *Earth and Planetary Science Letters*, *102*(3), 395–412. https://doi.org/10.1016/0012-821X(91)90031-C

Scrocca, D. (2010). Southern Apennines: Structural setting and tectonic evolution. *Journal of the Virtual Explorer*, *36*. https://doi.org/10.3809/jvirtex.2010.00225

Scrocca, D., Carminati, E., & Doglioni, C. (2005). Deep structure of the southern Apennines, Italy: Thin-skinned or thick-skinned? *Tectonics*, *24*(3), TC3005. https://doi.org/10.1029/2004TC001634

Scrocca, D., Doglioni, C., & Innocenti, F. (2003). Constraints for an interpretation of the Italian geodynamics: A review. *62*, 15–46.

Segall, P. (1989). Earthquakes triggered by fluid extraction. *Geology*, *17*(10), 942–946. https://doi.org/10.1130/0091-7613(1989)017⟨0942:ETBFE⟩2.3.CO;2

Serlenga, V., & Stabile, T. A. (2019). How do local earthquake tomography and inverted dataset affect earthquake locations? The case study of High Agri Valley (southern Italy). *Geomatics, Natural Hazards and Risk*, *10*(1), 49–78. https://doi.org/10.1080/19475705.2018.1504124

Serpelloni, E., Anzidei, M., Baldi, P., Casula, G., & Galvani, A. (2005). Crustal velocity and strain-rate fields in Italy and surrounding regions: New results from the analysis of permanent and non-permanent GPS networks. *Geophysical Journal International*, *161*(3), 861–880. https://doi.org/10.1111/j.1365-246X.2005.02618.x

Shiner, P., Beccacini, A., & Mazzoli, S. (2004). Thin-skinned versus thick-skinned structural models for Apulian carbonate reservoirs: Constraints from the Val d'Agri Fields, S Apennines, Italy. *Marine and Petroleum Geology*, *21*(7), 805–827. https://doi.org/10.1016/j.marpetgeo.2003.11.020

Shiner, P., Mazzoli, S., & Cello, G. (2004). Interactions between thin and thick-skinned thrusting in the Val d'Agri area of the S. Apennines. In *Paper presented at the 32nd international geological congress* (Vol. 21). International Union of Geological Sciences.

Sibson, H. (2000). Fluid involvement in normal faulting. *Journal of Geodynamics*, *29*(3–5), 469–499. https://doi.org/10.1016/S0264-3707(99)00042-3

Silverii, F., D'Agostino, N., Métois, M., Fiorillo, F., & Ventafridda, G. (2016). Transient deformation of karst aquifers due to seasonal and multi-year groundwater variations observed by GPS in southern Apennines (Italy). *Journal of Geophysical Research: Solid Earth*, *121*(11), 8315–8337. https://doi.org/10.1002/2016JB013361

Speranza, F., & Chiappini, M. (2002). Thick-skinned tectonics in the external Apennines, Italy: New evidence from magnetic anomaly analysis. *Journal of Geophysical Research*, *107*(B11), ETG8-1–ETG8-19. https://doi.org/10.1029/2000JB000027

Stabile, T. A., Giocoli, A., Lapenna, V., Perrone, A., Piscitelli, S., & Telesca, L. (2014). Evidence of low-magnitude continued reservoir-induced seismicity associated with the Pertusillo artificial lake (southern Italy). *Bulletin of the Seismological Society of America*, *104*(4), 1820–1828. https://doi.org/10.1785/0120130333

Stabile, T. A., Giocoli, A., Perrone, A., Piscitelli, S., & Lapenna, V. (2014). Fluid injection induced seismicity reveals a NE dipping fault in the southeastern sector of the High Agri Valley (southern Italy). *Geophysical Research Letters*, *41*(16), 5847–5854. https://doi.org/10.1002/2014GL060948

Stabile, T. A., Giocoli, A., Perrone, A., Piscitelli, S., Telesca, L., & Lapenna, V. (2015). Relationship between seismicity and water level of the Pertusillo reservoir (southern Italy). *Bollettino di Geofisica Teorica ed Applicata*, *56*, 505–517. https://doi.org/10.4430/bgta0161

Stabile, T. A., & Telesca, L. (2023). The statistical fingerprint of fluid-injection operations on microseismic activity at the Val d'Agri oil field (southern Italy). *Energies*, *16*(16), 5877. https://doi.org/10.3390/en16165877

Stabile, T. A., Vlček, J., Wcisło, M., & Serlenga, V. (2021). Analysis of the 2016–2018 fluid-injection induced seismicity in the High Agri Valley (southern Italy) from improved detections using template matching. *Scientific Reports*, *11*(1), 20630. https://doi.org/10.1038/s41598-021-00047-6

Stampfli, G. (2005). Plate tectonics of the Apulia-Adria microcontinents. *CROP Project-Deep Seismic Explorations of the Central Mediterranean and Italy, Section*, *11*, 747–766.

Stampfli, G., Borel, G., Marchant, R., & Mosar, J. (2002). Western Alps geological constraints on western Tethyan reconstructions. *Journal of the Virtual Explorer*, *8*. https://doi.org/10.3809/jvirtex.2002.00057

Stanchits, S., Mayr, S., Shapiro, S., & Dresen, G. (2011). Fracturing of porous rock induced by fluid injection. *Tectonophysics*, *503*(1), 129–145. (Thermo-Hydro-Chemo-Mechanical Couplings in Rock Physics and Rock Mechanics). https://doi.org/10.1016/j.tecto.2010.09.022

Steckler, M. S., Agostinetti, N. P., Wilson, C. K., Roselli, P., Seeber, L., Amato, A., & Lerner-Lam, A. (2008). Crustal structure in the southern Apennines from teleseismic receiver functions. *Geology*, *36*(2), 155–158. https://doi.org/10.1130/G24065A.1

Stein, S., & Sella, G. F. (2006). Pleistocene change from convergence to extension in the Apennines as a consequence of Adria microplate motion. In N. Pinter, G. Gyula, J. Weber, S. Stein, & D. Medak (Eds.), *The Adria microplate: GPS geodesy, tectonics and hazards* (pp. 21–34).

Sternai, P., Muller, V. A. P., Jolivet, L., Garzanti, E., Corti, G., Pasquero, C., et al. (2021). Effects of asthenospheric flow and orographic precipitation on continental rifting. *Tectonophysics*, *820*, 229120. https://doi.org/10.1016/j.tecto.2021.229120

Tallarico, A., Santini, S., & Dragoni, M. (2005). Stress changes due to recent seismic events in the central Apennines (Italy). *Pure and Applied Geophysics*, *162*(12), 2273–2298. https://doi.org/10.1007/s00024-005-2779-3

Talone, D., De Siena, L., Lavecchia, G., & de Nardis, R. (2023). The attenuation and scattering signature of fluid reservoirs and tectonic interactions in the central-southern Apennines (Italy). *Geophysical Research Letters*, *50*(22), e2023GL106074. https://doi.org/10.1029/2023GL106074

Telesca, L., Giocoli, A., Lapenna, V., & Stabile, T. (2015). Robust identification of periodic behavior in the time dynamics of short seismic series: The case of seismicity induced by Pertusillo Lake, southern Italy. *Stochastic Environmental Research and Risk Assessment*, *29–1446*(5), 1437–1446. https://doi.org/10.1007/s00477-014-0980-6

Thieulot, C. (2011). FANTOM: Two- and three-dimensional numerical modelling of creeping flows for the solution of geological problems. *Physics of the Earth and Planetary Interiors*, *188*(1–2), 47–68. https://doi.org/10.1016/j.pepi.2011.06.011

Toda, S., Stein, R. S., & Lin, J. (2011). Widespread seismicity excitation throughout central Japan following the 2011 m=9.0 Tohoku earthquake and its interpretation by Coulomb stress transfer. *Geophysical Research Letters*, *38*(7), L00G03. https://doi.org/10.1029/2011GL047834

Turrini, C., & Rennison, P. (2004). Structural style from the southern Apennines' hydrocarbon province—An integrated view. *Thrust Tectonics and Hydrocarbon Systems: AAPG Memoir*, *82*, 558–578.

Valoroso, L., Improta, L., Chiaraluce, L., Di Stefano, R., Ferranti, L., Govoni, A., & Chiarabba, C. (2009). Active faults and induced seismicity in the Val d'Agri area (southern Apennines, Italy). *Geophysical Journal International*, *178*(1), 488–502. https://doi.org/10.1111/j.1365-246X.2009.04166.x

Valoroso, L., Improta, L., De Gori, P., & Chiarabba, C. (2011). Upper crustal structure, seismicity and pore pressure variations in an extensional seismic belt through 3-D and 4-D V_p and V_p/V_s models: The example of the Val d'Agri area (southern Italy). *Journal of Geophysical Research*, *116*(B7), B07303. https://doi.org/10.1029/2010JB007661

Van Dinther, Y., Gerya, T., Dalguer, L., Mai, P., Morra, G., & Giardini, D. (2013). The seismic cycle at subduction thrusts: Insights from seismo-thermo- mechanical models. *Journal of Geophysical Research: Solid Earth*, *118*(12), 6183–6202. https://doi.org/10.1002/2013JB010380

Van Zelst, I., Crameri, F., Pusok, A. E., Glerum, A., Dannberg, J., & Thieulot, C. (2022). 101 geodynamic modelling: How to design, interpret, and communicate numerical studies of the solid Earth. *Solid Earth*, *13*(3), 583–637. https://doi.org/10.5194/se-13-583-2022

Vogt, K., Castro, A., & Gerya, T. (2013). Numerical modeling of geochemical variations caused by crustal relamination. *Geochemistry, Geophysics, Geosystems*, *14*(2), 470–487. https://doi.org/10.1002/ggge.20072

Waltham, D. (1992). Mathematical modelling of sedimentary basin processes. *Marine and Petroleum Geology*, *9*(3), 265–273. https://doi.org/10.1016/0264-8172(92)90075-P

Yerkes, R. F., & Castle, R. O. (1976). Seismicity and faulting attributable to fluid extraction. *Engineering Geology*, *10*(2), 151–167. https://doi.org/10.1016/0013-7952(76)90017-X

Yoon, J. S., Stephansson, O., Zang, A., Min, K.-B., & Lanaro, F. (2017). Discrete bonded particle modelling of fault activation near a nuclear waste repository site and comparison to static rupture earthquake scaling laws. *International Journal of Rock Mechanics and Mining Sciences*, *98*, 1–9. https://doi.org/10.1016/j.ijrmms.2017.07.008

Zembo, I. (2010). Stratigraphic architecture and quaternary evolution of the Val d'Agri intermontane basin (southern Apennines, Italy). *Sedimentary Geology*, *223*(3), 206–234. https://doi.org/10.1016/j.sedgeo.2009.11.011